

Modeling oxygen-void interactions in uranium nitride

Mohamed AbdulHameed^a, Anton J. Schneider^b, Benjamin Beeler^{a,c,*}, Michael W.D. Cooper^{b,**}

^a*Department of Nuclear Engineering, North Carolina State University, Raleigh, NC 27695*

^b*Los Alamos National Laboratory, Los Alamos, NM 87545*

^c*Idaho National Laboratory, Idaho Falls, ID 83415*

Abstract

Oxygen impurities in uranium nitride (UN) are reported to influence its swelling behavior under irradiation, yet the underlying mechanism remains unknown. In this work, we develop a first-principles model that quantifies the interaction of oxygen with voids and fission gas bubbles in UN, leading to a reduction in surface energy that can promote swelling. The analysis reveals that segregation of substitutional oxygen at surface nitrogen sites is the primary driver of surface energy reduction, $|\Delta\sigma|$, while oxygen in surface hollow sites plays a minor and sometimes counteracting role. $|\Delta\sigma|$ is most pronounced for small cavities ($R_v = 1\text{--}10 \text{ nm}$) at intermediate temperatures that coincide with the onset of breakaway swelling in UN. Larger voids require higher temperatures for oxygen adsorption to significantly lower their surface energy. The temperature dependence of $|\Delta\sigma|$ exhibits three regimes: negligible reduction at low temperatures due to sluggish oxygen diffusion, a maximum at intermediate temperatures where oxygen incorporation is optimal, and a decline at high temperatures due to enhanced bulk solubility. A parametric analysis reveals that $|\Delta\sigma|$ depends strongly on both oxygen concentration and cavity size, but is largely insensitive to porosity. Our results suggest that oxygen-induced surface energy reduction is essential for reconciling the mechanistic swelling model of UN with experimental observations.

Keywords: Uranium nitride, Oxygen segregation, Surface energy reduction, Void nucleation, Fission gas swelling

*Corresponding author

**Corresponding author

Email addresses: bwbeeler@ncsu.edu (Benjamin Beeler), cooper_m@lanl.gov (Michael W.D. Cooper)

¹ **1. Introduction**

² Uranium nitride (UN) is considered a highly promising fuel for fast nuclear reactors,
³ space reactors, and potentially commercial light water reactors, due to its high uranium
⁴ density and high thermal conductivity relative to UO_2 [1, 2]. However, early use of UN
⁵ was limited by issues such as rapid oxidation in air, poor tolerance to water and steam,
⁶ difficulty in sintering, and the need for nitrogen enrichment with N-15 due to the high neutron
⁷ absorption of N-14 [1, 2]. Furthermore, many aspects of its behavior at high temperatures and
⁸ under irradiation remain poorly understood, with scarce experimental data and incomplete
⁹ mechanistic pictures [1, 2]. Several studies have sought to address this knowledge gap by,
¹⁰ for instance, offering an atomistic-level understanding of the deformation mechanisms in
¹¹ UN [3, 4], which play a critical role in pellet-clad mechanical interactions. Additionally, a
¹² mechanistic multiscale model has been developed to describe its swelling behavior [5].

¹³ UN experiences pronounced swelling driven by the growth of fission gas bubbles to sizes
¹⁴ larger than those observed in UO_2 [5–7], making dimensional stability a key concern for
¹⁵ this fuel. The mechanistic model by Rizk *et al.* [5] gives a multiscale description of fission-
¹⁶ gas swelling and release in UN, coupling atomistic defect data to the BISON finite-element
¹⁷ framework via the Simple Integrated Fission Gas Release and Swelling (SIFGRS) model.
¹⁸ Their calculations, however, employed a constant void/bubble surface energy derived for
¹⁹ oxygen-free UN.

²⁰ A major challenge in utilizing UN as a nuclear fuel is the presence of oxygen impurities,
²¹ which can markedly affect its swelling characteristics. Rogozkin *et al.* [8] demonstrated
²² that fuel swelling becomes substantially more pronounced when the oxygen concentration
²³ in UN surpasses the range of 1000 to 1500 parts per million (ppm). Consequently, Schuler
²⁴ *et al.* [9] recommended limiting the maximum permissible oxygen content to 1000–1500
²⁵ ppm to maintain dependable performance of fuel elements. Nevertheless, achieving UN
²⁶ powders with oxygen levels below 1500 ppm has thus far only been accomplished under
²⁷ controlled laboratory conditions [9]. This highlights the importance of investigating how
²⁸ oxygen interacts with UN’s microstructural features, like voids and bubbles.

²⁹ Additionally, mechanistic models that aim to predict fission gas swelling in UN require
³⁰ knowledge of surface energies. Surface energy is a core input to the SIFGRS model utilized
³¹ by Rizk *et al.* [5] as it sets both the equilibrium pressure inside a bubble as a function of its
³² radius, and the contact angle of intergranular bubbles. Therefore, understanding whether
³³ oxygen significantly alters the surface energy of voids or gas bubbles is essential for accurately
³⁴ modeling swelling behavior.

³⁵ The effect of light impurities, such as oxygen, on vacancy cluster morphology has been
³⁶ extensively studied in metals like copper, nickel, and stainless steel [10–13]. These studies
³⁷ have utilized elastic continuum models [10, 11], thermodynamic models [12], and reaction
³⁸ rate theory [13] to understand the interaction between impurities and void embryos among
³⁹ other vacancy cluster types. Usually, oxygen impurities impact swelling in metals and alloys
⁴⁰ by segregating around void surfaces, lowering their surface energy, thereby reducing the
⁴¹ critical void radius in the void nucleation stage [10, 13]. Experimental evidence from metal
⁴² studies supports the notion that oxygen reduces the surface energy of small voids, typically
⁴³ around 50 vacancies [12]. This reduction in surface energy is a key factor in stabilizing
⁴⁴ voids and fission-gas bubbles and may similarly affect the swelling behavior in UN. More

45 strikingly, the theoretical studies by Zinkle *et al.* [10, 11] predict that void formation in
46 high-purity metals is energetically unfavorable, and impurities like oxygen are essential for
47 voids to form. That is, void formation is greatly reduced or even suppressed in low-oxygen
48 metals and alloys. It has been further suggested that oxygen might stabilize void embryos
49 by preventing their collapse into dislocation loops, even if it does not directly reduce surface
50 energy [11, 12].

51 Several first-principles studies have explored the properties of oxygen impurities in bulk
52 UN and on its surfaces, calculating the oxygen incorporation, migration, and adsorption
53 energies [9, 14–23]. These studies have demonstrated that oxygen atoms prefer to incorpo-
54 rate into pre-existing nitrogen vacancies, both in bulk UN and on the surface, rather than
55 occupying tetrahedral interstitial sites [14, 20]. Oxygen impurities also reduce the migra-
56 tion energy of nearby nitrogen vacancies [15], indicating that oxygen can influence behaviors
57 that depend on defect dynamics, such as creep. Additionally, it has been observed that O₂
58 molecules parallel to the (001) surface can spontaneously dissociate when centered over a
59 hollow site or a nitrogen atom [16].

60 A particularly relevant study on the effect of oxygen on swelling in UN is that by Schuler *et*
61 *al.* [9], who investigated the thermodynamic and transport properties of oxygen in UN using
62 a self-consistent mean-field (SCMF) model. The input energies for their model were derived
63 from density functional theory with the addition of a Hubbard U term (DFT+ U). Schuler
64 *et al.* found that oxygen is thermodynamically more favorable in the bulk of UN rather than
65 on the (001) surface, leading them to conclude that oxygen segregation on surfaces would
66 be driven by kinetic factors rather than by thermodynamics. However, Kocevski *et al.* [24]
67 later demonstrated that UN modeled using DFT+ U exhibits imaginary phonon frequencies,
68 indicating a dynamically unstable crystal structure. Consequently, the defect energetics used
69 in the SCMF model by Schuler *et al.* might need reconsideration.

70 Oxygen occurs in fresh UN fuel in solution or as a separate UO₂ phase, dependent on
71 O concentration and temperature [25]. UO₂ precipitates have been observed experimentally
72 in regions of UN samples where the local oxygen concentration apparently exceeded the
73 solubility limit [26]. Additionally, DFT studies indicate that oxygen interaction with UN
74 surfaces can lead to the formation of oxynitrides (UO_xN_y) or pseudo-UO₂ structures [20, 21].

75 In this work, we use DFT data to parametrize a thermodynamic model based on defect
76 reactions to study how oxygen impurities interact with voids and fission-gas bubbles in UN.
77 Our model focuses on oxygen adsorption onto void surfaces, where it may reduce surface
78 energy and potentially influence swelling. Throughout this work, we assume that inert gas
79 atoms have no impact on surface energy; therefore, the surface energies of voids and fission-
80 gas bubbles are considered identical. To the best of our knowledge, this is the first study
81 that attempts to quantify the extent to which oxygen interaction with void surfaces affects
82 the void nucleation behavior in UN. We assume that oxygen is the only impurity present,
83 and do not account for the formation of UO₂. These simplifications allow us to concentrate
84 on the primary thermodynamic factors that govern the interaction of oxygen with voids,
85 providing an initial step toward understanding the role of oxygen in UN swelling.

86 **2. Methodology**

87 *2.1. DFT calculations*

88 DFT calculations performed in this work utilize the Vienna Ab-initio Simulation Package
 89 (VASP) [27–29] using the Perdew-Burke-Ernzerhof (PBE) [30] generalized gradient approxi-
 90 mation (GGA) to the exchange-correlation (XC) functional. The pseudopotential models of
 91 uranium, nitrogen, and oxygen are based on the projector augmented wave (PAW) method
 92 [31] where the valence electron configuration of U is $6s^2 6p^6 6d^2 5f^2 7s^2$ (14 electrons), that
 93 of N is $2s^2 2p^3$ (5 electrons), and that of O is $2s^2 2p^4$ (6 electrons). Methfessel and Paxton’s
 94 smearing method [32] of the first order is used with a width of 0.1 eV to determine the partial
 95 occupancies for each wavefunction. $3 \times 3 \times 3$ supercells of ferromagnetic (FM) UN are used
 96 to model bulk UN and to study the properties of defects and impurities. To study surface
 97 properties, 6-layer and 8-layer symmetric slabs of FM UN are used, where the vacuum gap
 98 in each is twice the length of the slab along the z-direction. It was shown by Kocevski *et al.*
 99 [24] that the FM ordering provides a suitable model of UN at 0 K. Brillouin zone sampling is
 100 performed using Monkhorst-Pack [33] $3 \times 3 \times 3$ and $3 \times 3 \times 1$ k -point meshes for the $3 \times 3 \times 3$
 101 supercells and the symmetric slabs, respectively. In all energy minimization calculations,
 102 we set the cutoff energy of the plane-wave basis as 520 eV, the electronic relaxation conver-
 103 gence criterion as 10^{-4} eV, and the ionic relaxation convergence criterion as 10^{-2} eV/Å. The
 104 nudged elastic band (NEB) method [34] with the climbing image algorithm [35] is used to
 105 calculate the migration energies of O_i and $\{O_N : v_N\}$. The structures and ionic minimization
 106 trajectories are visualized using OVITO [36] and VESTA [37].

107 Point defect formation energies are calculated from:

$$E_f = E_d - E_p - \sum_i n_i \mu_i, \quad (1)$$

108 where E_d and E_p are the energies of the supercell with and without the defect, respectively,
 109 n_i is the number of atoms of type i removed ($n_i < 0$) or added ($n_i > 0$) to form the defect,
 110 and μ_i is the chemical potential of the i th species.

111 The U and N chemical potentials are calculated from [38]:

$$E_c(U_xN_y) = x\mu_U + y\mu_N, \quad (2)$$

112 where $E_c(U_xN_y)$ is the cohesive energy (energy per formula unit) of compound U_xN_y . Eq. (2)
 113 is solved for UN and α -U to get the U-rich chemical potentials, and for UN and α - U_2N_3 to
 114 get the N-rich chemical potentials [39, 40]. The chemical potentials at the intermediate
 115 near-stoichiometric conditions are the averages of these two bounds [41].

116 The binding energy of a defect cluster $\{A_X : B_Y\}$ is calculated from:

$$E_b = E(\{A_X : B_Y\}) + E_p - E(A_X) - E(B_Y), \quad (3)$$

117 where $E(\cdot)$ is the energy of the supercell containing the relevant defect. Based on this
 118 formulation, a negative E_b means binding is favorable.

119 The incorporation energy of an impurity B in a defect v_X to form B_X is calculated from:

$$E_{inc} = E(B_X) - E(v_X) - \mu_B, \quad (4)$$

120 where μ_B is the chemical potential of the impurity in its reference state. The oxygen chemical
 121 potential is discussed in [Section 2.2](#). Note that $E(v_i) = E_p$, where v_i denotes a vacant
 122 interstitial site.

123 The surface energy is calculated from [\[42\]](#):

$$\sigma = \frac{1}{A} \left(E^* - \sum_i N_i \mu_i \right), \quad (5)$$

124 where E^* is the total DFT energy of the supercell containing the surface, A is the total
 125 surface area, N_i is the number of atoms of species i in the supercell containing the surface,
 126 and μ_i is the corresponding chemical potential. Note that $i \in \{\text{U, N, O}\}$.

127 The adsorption energy is calculated from:

$$E_{\text{ad}} = \frac{1}{N_{\text{ad}}} (E_{\text{surf+ad}} - E_{\text{surf}}) - \mu_{\text{ad}}, \quad (6)$$

128 where $E_{\text{surf+ad}}$ and E_{surf} are the energies of the symmetric slabs with and without the ad-
 129 sorbed atom(s), N_{ad} is the number of adsorbed atoms, and μ_{ad} is their chemical potential.

130 Finally, it is of interest to estimate the change in the surface energy upon oxygen ad-
 131 sorption or surface defect formation. This is accomplished by using the following expression,
 132 which is derived in [Appendix B](#):

$$\Delta\sigma = \frac{8}{3} \frac{1-p}{p} \frac{R_v}{a^3} c_O \left[\alpha_1 \frac{[\text{O}_N^{(\text{s})}]}{[\text{O}_N^{(\text{b})}]} E_{\text{ad}}(\text{O}_N^{(\text{s})}) + \alpha_2 \frac{[\text{O}_i^{(\text{s})}]}{[\text{O}_N^{(\text{b})}]} E_{\text{ad}}(\text{O}_i^{(\text{s})}) \right] + \frac{2}{a^2} [v_N^{(\text{s})}] E_f(v_N^{(\text{s})}), \quad (7)$$

133 where p is the porosity, R_v is the average void radius, a is the lattice constant, c_O is the
 134 atomic oxygen concentration, and α_1 and α_2 are the kinetic corrections for the defects $\text{O}_N^{(\text{s})}$
 135 and $\text{O}_i^{(\text{s})}$, respectively. For a defect i , α_i is defined as [\[12\]](#):

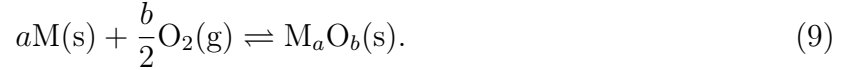
$$\alpha_i = \begin{cases} \sqrt{D_i t} / \lambda_v & \text{if } \sqrt{D_i t} / \lambda_v < 1, \\ 1 & \text{if } \sqrt{D_i t} / \lambda_v \geq 1, \end{cases} \quad (8)$$

136 where D_i is the diffusivity of the relevant defect, t is the void nucleation time, and λ_v is
 137 the mean free path between voids, defined as $\lambda_v = n_v^{-1/3}$, where $n_v = p / (\frac{4}{3} \pi R_v^3)$ is the void
 138 number density. We assume a void nucleation time $t = 42$ hours. This estimate is justified
 139 by taking a typical dose rate, \dot{G} , in a fast reactor core as on the order of 10^{-6} dpa/s [\[43, 44\]](#).
 140 In stainless steels, stable voids are fully formed by a dose, G , in the range of 0.1–0.2 dpa [\[45\]](#).
 141 Using the relation $t = G/\dot{G}$, this corresponds to a void nucleation time between 28 and 56
 142 hours, with an average of 42 hours. Due to the lack of experimental data on early-stage
 143 void nucleation in UN fuels, this estimated time serves as a reasonable placeholder, but with
 144 unknown uncertainty. Note that [Eq. \(7\)](#) predicts that the surface energy reduction scales
 145 linearly with oxygen concentration.

146 2.2. Oxygen chemical potential

147 DFT calculations with GGA exchange-correlation functionals are known for being inaccu-
 148 rate for gases like O_2 [\[20\]](#). This is usually remedied by using hybrid functionals or applying

¹⁴⁹ semi-empirical corrections [46]. Alternatively, Finnis *et al.* [42] suggested using common
¹⁵⁰ oxides as the oxygen reference state. For an oxide M_aO_b , the formation reaction is:



¹⁵¹ The Gibbs free energy balance for this reaction is:

$$\Delta_f G^0(M_aO_b) = g^0(M_aO_b) - a\mu_M^0 - b\mu_O^0, \quad (10)$$

¹⁵² where $\Delta_f G^0(M_aO_b)$ is the standard Gibbs free energy of formation for the oxide, which is
¹⁵³ available in thermochemical tables [47], $g^0(M_aO_b)$ is approximated by the DFT energy per
¹⁵⁴ formula unit of the oxide, μ_M^0 is approximated by the DFT energy per atom of the metal,
¹⁵⁵ and μ_O^0 is the oxygen chemical potential. The superscript 0 on any quantity denotes its
¹⁵⁶ value at the standard pressure, $P^0 = 1$ bar, and standard temperature, $T^0 = 298.15$ K.
¹⁵⁷ Approximating T^0 with 0 K in the context of DFT calculations introduces little error [42].
¹⁵⁸ Rearranging Eq. (10), the oxygen chemical potential is:

$$\mu_O^0 = \frac{1}{b} [g^0(M_aO_b) - a\mu_M^0 - \Delta_f G^0(M_aO_b)]. \quad (11)$$

¹⁵⁹ Finnis *et al.* state that the chemical potential of oxygen should be independent of the
¹⁶⁰ specific oxide used. Using MgO and Al₂O₃ as the initial oxide, we found that the chemical
¹⁶¹ potential for both is $\mu_O = -4.18$ eV. This value is used as the reference chemical potential
¹⁶² to report all the oxygen incorporation and adsorption energies in Section 3. However, we are
¹⁶³ concerned with studying how oxygen interacts with voids in UN, where oxygen atoms are
¹⁶⁴ introduced as impurities during manufacturing. For this setting, the oxygen reference state
¹⁶⁵ is not the oxide, but rather the most dominant oxygen impurity type, which is O_N^(b) as will
¹⁶⁶ be shown in Section 3. Note that we use the Kröger-Vink notation [48] to describe point
¹⁶⁷ defects, but with charges omitted because UN exhibits metallic properties and defects have
¹⁶⁸ no associated charge [49]. Superscripts (b) and (s) are added to the Kröger-Vink notation
¹⁶⁹ to differentiate bulk and surface defects, respectively.

¹⁷⁰ The reference state of oxygen impurities in UN is based on the following defect reaction:



¹⁷¹ which has the following mass-action law:

$$K_1 = \frac{[O_N^{(b)}]}{[v_N^{(b)}]P_{O_2}^{1/2}} = \exp\left[-\frac{E(O_N) - E(v_N)}{kT}\right], \quad (13)$$

¹⁷² where $E(O_N)$ and $E(v_N)$ are the DFT energies of the supercells containing O_N and v_N , respec-
¹⁷³ tively. This difference is termed the “raw incorporation energy” [38], i.e., the incorporation
¹⁷⁴ energy without considering the impurity’s reference state. The dependence of the oxygen
¹⁷⁵ chemical potential on oxygen partial pressure, P_{O_2} , and temperature, T , is given by [42]:

$$\mu_O(P_{O_2}, T) = g(T) + \frac{1}{2}kT \ln(P_{O_2}/P^0), \quad (14)$$

¹⁷⁶ where the temperature dependence, $g(T)$, is extracted from thermochemical tables [47].
¹⁷⁷ Focusing on the dependence on the oxygen partial pressure:

$$\mu_O(P_{O_2}) = \frac{1}{2}kT \ln\left(\frac{P_{O_2}}{P^0}\right), \quad (15)$$

¹⁷⁸ and rearranging Eqs. (13) and (15), it can be easily shown that the oxygen chemical potential
¹⁷⁹ is:

$$\mu_O = E(O_N) - E(v_N) + kT \ln\left(\frac{[O_N^{(b)}]}{[v_N^{(b)}]}\right). \quad (16)$$

¹⁸⁰ 2.3. Oxygen diffusivity

¹⁸¹ The diffusivity of oxygen impurities is also explored in this work. The diffusivity of a
¹⁸² defect d is calculated from:

$$D_d = \frac{1}{6}z\lambda^2\nu \exp\left(-\frac{E_m}{kT}\right), \quad (17)$$

¹⁸³ where $d \in \{O_i, \{O_N:v_N\}\}$, z is the number of equivalent sites the atom can jump to, and λ
¹⁸⁴ is the jump distance. Both z and λ are determined from the crystal structure. For O_i , $z =$
¹⁸⁵ 6 and $\lambda = a/2$, with a being the lattice constant. For $\{O_N:v_N\}$, $z = 12$ and $\lambda = a/\sqrt{2}$. E_m
¹⁸⁶ is the effective migration energy. For O_i , $E_m = 2.41$ eV. For $\{O_N:v_N\}$, net bulk diffusion
¹⁸⁷ requires two steps [50]: (a) O_N and v_N exchange, and (b) v_N rotation around O_N . Note the
¹⁸⁸ O_N is immobile by itself and can only move via this two-step process with the assistance
¹⁸⁹ of a nearby v_N . The saddle point energy of the exchange step is 2.87 eV, whereas that of
¹⁹⁰ the rotation step is 3.06 eV. Based on the highest barrier approximation [51], the effective
¹⁹¹ migration energy is 3.06 eV.

¹⁹² In Eq. (17), ν is the attempt frequency, which can be estimated from phonon calculations.
¹⁹³ Because these calculations are computationally expensive, we use a semi-classical approach
¹⁹⁴ to estimate ν as [52]:

$$\nu = \left(\frac{E_m}{2m\lambda^2}\right)^{1/2}, \quad (18)$$

¹⁹⁵ where m is the mass of the diffusing atom. For $\{O_N:v_N\}$, the limiting step is the rotation of
¹⁹⁶ v_N around O_N and the mass of the nitrogen atom is used. For O_i , the mass of the oxygen atom
¹⁹⁷ is used. For the diffusion of $\{O_N:v_N\}$, $\nu = 9.45 \times 10^{12}$ Hz, whereas for O_i , $\nu = 1.11 \times 10^{13}$
¹⁹⁸ Hz.

¹⁹⁹ The diffusivity of an impurity X by a mechanism that depends on defect d is calculated
²⁰⁰ from [49]:

$$D_{X,d} = f \frac{c_d}{c_X} D_d, \quad (19)$$

²⁰¹ where f is the correlation factor. For $\{O_N:v_N\}$, $f = 0.7815$ [53], which is the value for
²⁰² vacancy-mediated migration in the FCC nitrogen sublattice. For O_i , $f = 1$ [53]. c_d is the
²⁰³ atomic concentration of the defect d and c_X is the total atomic concentration of impurity X.
²⁰⁴ As an approximation, we assume that $c_O = [O_N]$ which will be justified in Section 3.3 of the
²⁰⁵ results.

206 2.4. Defect reactions

207 In this section, we outline the defect reactions used to estimate the relative concentrations
 208 of various oxygen defect types. In general, there are three categories of defect reactions: (a)
 209 reactions that relate defects in the bulk, (b) reactions that relate defects on the void surfaces,
 210 and (c) reactions that thermodynamically dictate defect transitions from the bulk to the void
 211 surfaces, and vice versa. A limitation of the latter category of reactions is that it neglects
 212 the kinetic aspects of the defect transitions. That is, the kinetics of reactions in (c) category
 213 are assumed to be faster than those in the (a) and (b) categories.

214 The first bulk defect reaction is:



215 and its mass-action law is:

$$K_2 = \frac{[O_i^{(b)}][v_N^{(b)}]}{[O_N^{(b)}]} = \exp \left[-\frac{E_{inc}(O_i^{(b)}) - E_{inc}(O_N^{(b)})}{kT} \right]. \quad (21)$$

216 The second bulk defect reaction is:



217 and its mass-action law is:

$$K_3 = \frac{\{\{O_N:v_N\}^{(b)}\}}{[v_N^{(b)}][O_N^{(b)}]} = \exp \left[-\frac{E_b(\{O_N:v_N\}^{(b)})}{kT} \right]. \quad (23)$$

218 The defect reaction at void surfaces is:



219 and its mass-action law is:

$$K_4 = \frac{[v_N^{(s)}][O_i^{(s)}]}{[v_i^{(s)}][O_N^{(s)}]} = \exp \left[-\frac{E_{ad}(O_i^{(s)}) - E_{ad}(O_N^{(s)})}{kT} \right]. \quad (25)$$

220 The first reaction that relates bulk UN and the void surface is:



221 and its mass-action law is:

$$K_5 = \frac{[v_N^{(s)}][N_N^{(b)}]}{[v_N^{(b)}][N_N^{(s)}]} = \exp \left[-\frac{E_f(v_N^{(s)}) - E_f(v_N^{(b)})}{kT} \right]. \quad (27)$$

222 $[N_N^{(s)}]$, the atomic concentration of the nitrogen sites on the surface, can be estimated from
 223 knowledge of the porosity, p , and the average void radius, R_v by the following expression
 224 which is derived in [Appendix A](#):

$$[N_N^{(s)}] = \frac{3}{2} \frac{p}{1-p} \frac{a}{R_v}, \quad (28)$$

225 where a is the lattice constant. Note that $[N_N^{(b)}] = 1 - [N_N^{(s)}]$.

226 The second reaction is:



227 and its mass-action law is:

$$K_6 = \frac{[v_i^{(s)}][O_N^{(b)}]}{[v_N^{(b)}][O_i^{(s)}]} = \exp \left[-\frac{E_{\text{inc}}(O_N^{(b)}) - E_{\text{ad}}(O_i^{(s)})}{kT} \right]. \quad (30)$$

228 As derived in [Appendix A](#), $[v_i^{(s)}]$ is given by:

$$[v_i^{(s)}] = \frac{3p}{1-p} \frac{a}{R_v}. \quad (31)$$

229 To find the relative concentration $[O_N^{(s)}]/[O_N^{(b)}]$, it is not necessary to resort to a defect
230 reaction. Instead, the ratio is calculated from:

$$\frac{[O_N^{(s)}]}{[O_N^{(b)}]} = \frac{[O_i^{(s)}]}{[O_N^{(b)}]} \div \frac{[O_i^{(s)}]}{[O_N^{(s)}]} = \frac{[v_N^{(s)}]}{[v_N^{(b)}]} \exp \left[-\frac{E_{\text{ad}}(O_N^{(s)}) - E_{\text{inc}}(O_N^{(b)})}{kT} \right]. \quad (32)$$

231 3. Results

232 3.1. Defect energetics

233 The formation energies of U and N vacancies in UN are shown in [Table 1](#). The bulk
234 formation energies compare very well with those calculated by Yang and Kaltsoyannis [\[40\]](#)
235 and Kocevski *et al.* [\[24\]](#). It is noticed that there is a consistent difference of about 0.76 eV
236 between N vacancy formation on the surface and in the bulk, independent of stoichiometry.
237 This difference is termed the segregation energy of the N vacancy. It is easier to form an
238 N vacancy on the surface than in the bulk, and the number of $v_N^{(s)}$ sites is limited by the
239 available surface area.

Table 1: Formation energies (eV) of U and N vacancies in UN. Reference energies are DFT values calculated by Yang and Kaltsoyannis [\[40\]](#) and Kocevski *et al.* [\[24\]](#).

	U-rich		Intermediate		N-rich	
	Calc.	Ref.	Calc.	Ref.	Calc.	Ref.
$v_U^{(b)}$	3.28	3.17–3.43 [40] , 3.27–3.86 [24]	2.79	2.75–3.01 [40]	2.30	2.34–2.60 [40] , 2.09–2.58 [24]
$v_N^{(b)}$	1.64	1.76–1.90 [40] , 0.62–1.86 [24]	2.13	2.18–2.31 [40]	2.62	2.59–2.72 [40] , 1.42–2.82 [24]
$v_N^{(s)}$	0.88	—	1.37	—	1.86	—

240 The incorporation energies of oxygen in UN are shown in [Table 2](#), all given relative to
241 $\mu_O = -4.18$ eV. The most favorable oxygen defect in the bulk is O_N followed by O_i . We also
242 attempted to calculate the incorporation energy of the $\langle 111 \rangle$ and $\langle 110 \rangle$ O-N dumbbells. The
243 $\langle 111 \rangle$ O-N dumbbell has a larger incorporation energy (−1.11 eV) than the tetrahedral site,
244 whereas the $\langle 110 \rangle$ O-N dumbbell is unstable and relaxes to the $\langle 111 \rangle$ configuration. The
245 largest incorporation energy is that of O_U , which indicates that O impurities exist almost
246 exclusively in the N-sublattice.

Table 2: Incorporation energies of oxygen in UN for $\mu_O = -4.18$ eV. This value of μ_O is calculated according to the Finnis *et al.* [42] oxide method.

Defect	Incorporation energy [eV]
O_N	-7.23
O_i	-2.94
$\langle 111 \rangle$ O-N dumbbell	-1.11
$\langle 110 \rangle$ O-N dumbbell	Unstable
O_U	-0.40

The binding energies of the explored defect clusters are shown in **Table 3**, where negative values indicate favorable binding. The most relevant defect cluster to our study, i.e., $\{O_N : v_N\}$, has a binding energy of 0.03 eV, which is practically zero. That is, binding is neither favorable nor unfavorable, and the N vacancy can roam around independently of O_N . On the other hand, we found a strong tendency for binding between O_N and v_U , Kr_U , and Xe_U , all with an average binding energy of about -0.4 eV. We propose that this binding may promote the initial aggregation of defects into void or bubble embryos. This finding is consistent with experimental observations by Turos *et al.* [54], who reported that Kr and Xe atoms form impurity-defect complexes in UN, serving as precursors for gas bubble formation. A comparable phenomenon is observed with helium in copper [11], where helium does not reduce the void surface energy but stabilizes void embryos by binding with vacancies and vacancy clusters. A similar role may be played by oxygen in UN, potentially contributing to the stabilization of voids and bubbles. Due to the low concentrations of Kr_U and Xe_U , we anticipate that this effect is less significant than the direct reduction of surface energy through oxygen adsorption.

Table 3: Binding energies of defect clusters in UN. Negative values mean that binding is favorable and vice versa.

Defect cluster	Binding energy [eV]
$\{O_N : v_N\}$	0.03
$\{O_N : v_U\}$	-0.40
$\{O_N : Kr_U\}$	-0.41
$\{O_N : Xe_U\}$	-0.39

The migration energies of defects relevant to this study are shown in **Table 4**. As can be expected, the migration energy of O_i is smaller than that of $\{O_N : v_N\}$, which is 3.06 eV based on the highest barrier approximation. It is predicted that the migration energy of v_N is slightly reduced from 3.10 to 3.06 eV when an O_N is in a first nearest neighbor position. A similar observation has been made by Kotomin *et al.* [15].

Table 4: Migration energies of some defects and/or migration paths in UN.

Defect and/or migration path	Migration energy [eV]
v_N	3.10
O_i	2.41
$O_N - v_N$ exchange	2.87
v_N rotation around O_N	3.06

267 *3.2. UN surface properties*

268 Upon relaxation, the 8-layer UN (001) surface undergoes a slight adjustment of the
 269 interlayer spacing, with the maximum interlayer spacing change remaining below 1%. The
 270 energy of the UN (001) surface under various stoichiometric conditions with and without
 271 defects is presented in [Table 5](#). It is evident that the surface energies of the 6-layer and 8-
 272 layer slabs are very similar, indicating that the 6-layer slab is sufficient to achieve a converged
 273 description of the UN (001) surface. Therefore, the 6-layer slab is used in all subsequent
 274 adsorption calculations. Several observations can be made regarding the impact of adsorption
 275 on surface energy. Introducing $O_i^{(s)}$ onto the pure 6-layer surface decreases its energy by
 276 0.182 J/m², irrespective of the stoichiometry. Furthermore, the surface energy of the 6-layer
 277 surface with $O_N^{(s)}$ is reduced relative to that of the 6-layer surface with $v_N^{(s)}$ by 0.256 J/m²,
 278 also independent of stoichiometry.

Table 5: Surface energies of the UN (001) surface in units of J/m² as calculated by [Eq. \(5\)](#).

	U-rich	Intermediate	N-rich
6-layer pure surface	1.586	1.586	1.586
8-layer pure surface	1.592	1.592	1.592
6-layer surface with $O_i^{(s)}$	1.404	1.404	1.404
6-layer surface with $v_N^{(s)}$	1.620	1.638	1.656
6-layer surface with $O_N^{(s)}$	1.364	1.382	1.400

299 The oxygen adsorption sites explored in this work are shown in [Fig. 1](#) generated using
 300 VESTA. Oxygen adsorption energies in different sites on the 6-layer slab are given in [Table 6](#).
 301 The most stable site is a N surface vacancy, followed by the hollow site, i.e., $O_i^{(s)}$, as was also
 302 found in previous studies [14, 20]. The adsorption energy of the oxygen in the hollow site
 303 does not change if the oxygen atoms are on one or both sides of the slab, which indicates the
 304 absence of any polarity effects. Thus, considering only one side of the slab is sufficient for
 305 obtaining accurate adsorption energies. Oxygen adsorption energy in a hollow site slightly
 306 decreases from -4.84 eV to -4.85 eV when an oxygen atom is introduced in a nearest
 307 neighbor hollow site and increases to -4.72 eV for 4 neighboring O atoms forming a square,
 308 which is due to the lateral repulsive interaction between closely packed oxygen adsorbate
 309 atoms. This suggests that the saturation coverage of oxygen is probably smaller than 1
 310 ($\theta_s < 1$). However, in this model, oxygen-oxygen interactions are neglected, and a saturation
 311 coverage of 1 is assumed for all impurity sites. If the actual saturation coverage was, say,
 312 $\theta_s = 0.5$, the effect of this would be to divide $[v_i^{(s)}]$ by 2, which is negligible on a log scale.

313 Note that the adsorption energy of O atoms in above-U sites is the same as that of O in
 314 a hollow site ([Table 6](#)). To confirm that the above-U site is stable, we shifted the oxygen
 315 atom by 0.2 Å toward the hollow site, and it relaxed back to the above-U site. One way to
 316 account for the above-U sites in our model is to multiply $[v_i^{(s)}]$ by 2, as outlined in [Appendix](#)
 317 [A](#). The bridge site is marked as unstable since oxygen atoms in this configuration relax to
 318 the above-U position. The largest adsorption energy is that of the above-N site (equivalent
 319 to a site on the U sublattice).

320 The oxygen adsorption energies in [Table 6](#) are reported with the chemical potential of
 321 oxygen taken from the oxide as the reference state (i.e., [Eq. \(11\)](#)). As explained earlier,
 322 however, the more appropriate oxygen reference state is oxygen pre-existing in UN as an

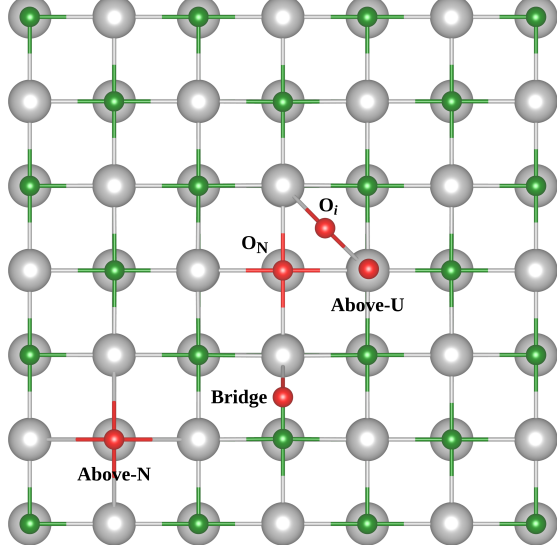


Figure 1: (Color online) A view of the UN surface along the z -axis (i.e., surface normal) showing the different oxygen adsorption sites. U atoms are gray, N atoms are green, and O atoms are red.

Table 6: Adsorption energy of oxygen into sites on the symmetric 6-layer slab model of the UN (001) surface. These values correspond to $\mu_O = -4.18$ eV, which is calculated according to the Finnis *et al.* [42] oxide method.

Adsorption site	Adsorption energy [eV]
$v_N^{(s)}$	-6.80
Hollow site (one side), i.e., $O_i^{(s)}$	-4.84
Hollow site (both sides)	-4.84
2 nearest-neighbor hollow sites (dumbbell)	-4.85
4 nearest-neighbor hollow sites (square)	-4.72
Bridge site	Unstable
Above-U site	-4.83
Above-N site	-2.77

303 impurity. In this case, the relevant chemical potential is that shown in Fig. C.10. The
 304 adsorption energies of oxygen relative to that chemical potential are shown in Figs. 2a and 2b
 305 for $O_N^{(s)}$ and $O_i^{(s)}$, respectively. Comparing these adsorption energies to those in Table 6, we
 306 can differentiate between two cases: While oxygen adsorption on external surfaces reduces
 307 surface energy both as $O_N^{(s)}$ and $O_i^{(s)}$, pre-existing oxygen in UN adsorbing on internal void
 308 surfaces reduces the surface energy only when adsorbing as $O_N^{(s)}$. In contrast, $O_i^{(s)}$ increases
 309 the surface energy of internal void surfaces. This behavior is due to the different reference
 310 states of oxygen in both cases.

311 3.3. Oxygen behavior

312 Several parameters must be defined to study the behavior of oxygen using our model.
 313 We assume an initial oxygen concentration of $w_O = 1500$ ppm, a porosity of $p = 5\%$, and
 314 an average void radius of $R_v = 1$ nm. The chosen $w_O = 1500$ ppm is the upper limit
 315 of the tolerated oxygen impurity concentration in UN [8, 9]. The optimal initial (closed)
 316 porosity for UN fuels to both suppress oxidation and accommodate gaseous fission products

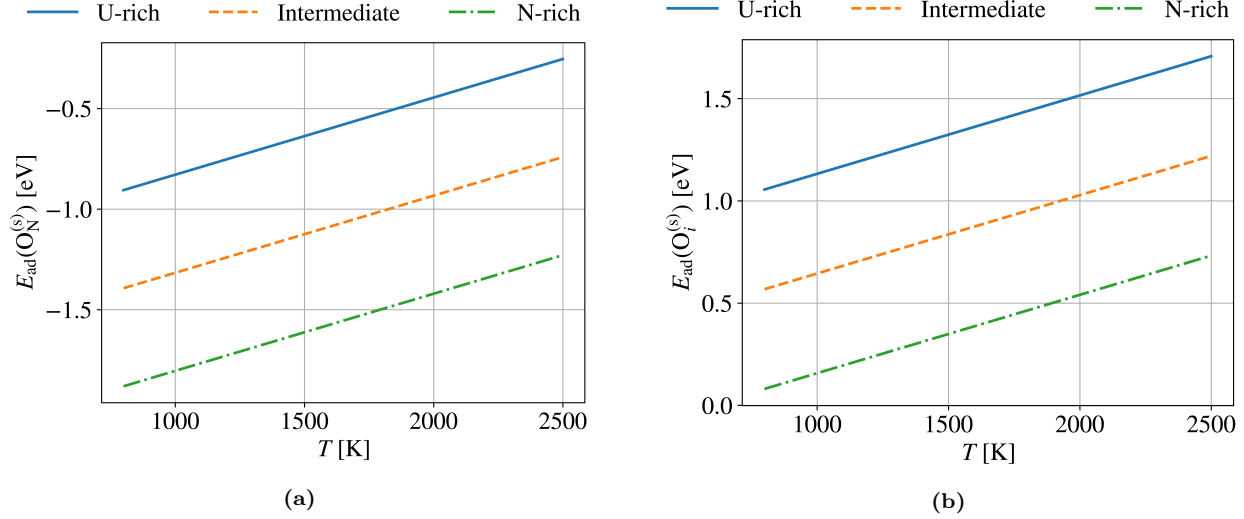


Figure 2: Temperature evolution of oxygen adsorption energy relative to the chemical potential shown in Fig. C.10 for (a) $O_N^{(s)}$ and (b) $O_i^{(s)}$.

is estimated to be 4% [55]. Note that the porosity in irradiated fuels is typically as high as 15% [56], which exceeds the 5% porosity assumed here. Lastly, the lower limit of reported fission gas bubble sizes in nitride and carbide fuels is close to $R_v = 1$ nm [57], which is also the critical void radius in metals [11].

The atomic concentrations of the N vacancy in the bulk and on the void surfaces are calculated with the aid of formation energies in Table 1 and Eq. (27) and are shown in Figs. C.9a and C.9b, respectively. The concentrations of $O_i^{(b)}$ and $\{O_N : v_N\}^{(b)}$, relative to $O_N^{(b)}$ are shown in Figs. 3a and 3b, respectively. It is clear that $O_N^{(b)}$ is the dominant defect type for oxygen impurities. Thus, it is justified to set $[O_N^{(b)}] \approx c_O$ where c_O is the atomic fraction of oxygen impurities, given by Eq. (B.14). $O_N^{(b)}$ is an immobile defect. Surface energy reduction requires O migration to void surfaces, which can only occur via the mobile defects $O_i^{(b)}$ and $\{O_N : v_N\}^{(b)}$. However, the immobile $O_N^{(b)}$ defects can stabilize void embryos via another mechanism by binding to v_U , Kr_U , and Xe_U , as explained earlier.

The relative concentration $[O_i^{(s)}]/[O_N^{(b)}]$ is illustrated in Fig. 4a. Under U-rich and intermediate conditions, this relative concentration exhibits Arrhenius behavior and remains relatively low. However, under N-rich conditions, which are more relevant in irradiation environments, the relative concentration is significantly higher and follows an anti-Arrhenius trend. Around 1600 K, for instance, for every ten oxygen atoms in the bulk, approximately one oxygen atom segregates to the surface as $O_i^{(s)}$. This behavior arises because, in N-rich environments, there are fewer nitrogen vacancies available to form $O_N^{(s)}$, leading to a preference for oxygen atoms to segregate to the surface. Similarly, in Fig. 4b, an anti-Arrhenius trend is also observed for the relative concentration $[O_N^{(s)}]/[O_N^{(b)}]$. This behavior is independent of stoichiometry, as it is solely governed by the segregation energy. As expected, this anti-Arrhenius behavior indicates that the solubility of oxygen in the bulk increases with increasing temperature. Lastly, Fig. 4c depicts the relative concentration $[O_i^{(s)}]/[O_N^{(s)}]$. As expected, $O_N^{(s)}$ is the dominant oxygen impurity site on the void surfaces. Interestingly, de-

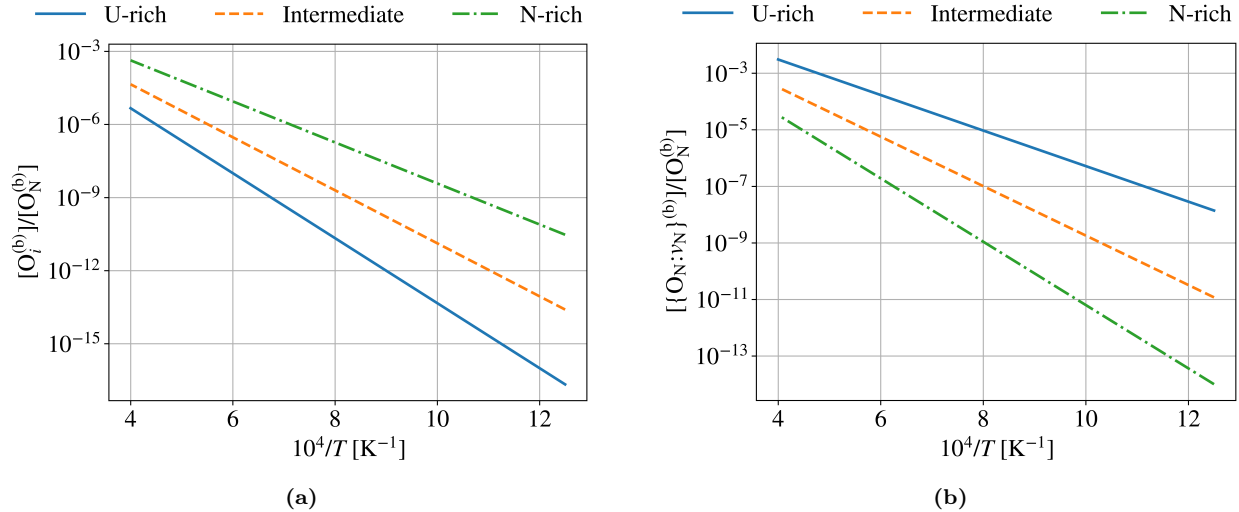


Figure 3: Relative concentrations of (a) $O_i^{(b)}$ and (b) $\{O_N:v_N\}^{(b)}$.

343 spite the large difference in adsorption energies, this relative concentration exceeds 0.1 in
 344 N-rich conditions across all considered temperatures.

345 The diffusivity of oxygen impurities in bulk UN through mechanisms dependent on the
 346 $\{O_N:v_N\}$ and O_i defects is illustrated in Fig. 5. Under U-rich conditions, the defect cluster
 347 $\{O_N:v_N\}$ dominates oxygen diffusion. This can be explained by the fact that U-rich envi-
 348 ronments have a higher concentration of nitrogen vacancies, allowing oxygen to exist as O_N
 349 in the bulk. These nitrogen vacancies also facilitate the diffusion process. In interme-
 350 diate conditions, both diffusion mechanisms are comparable, although O_i exhibits slightly higher
 351 diffusivity. In contrast, under N-rich conditions, the availability of nitrogen vacancies de-
 352 creases, and oxygen predominantly exists as an interstitial O_i . Consequently, the diffusion
 353 mechanism via O_i becomes dominant in this regime.

354 It is important to note that we assume $O_N^{(s)}$ defects reach the surface predominantly
 355 through the diffusion of $\{O_N:v_N\}$. This assumption is later utilized when calculating the
 356 reduction in surface energy due to surface adsorption. Specifically, the diffusivity used to
 357 calculate α_1 in Eq. (7) is that of $\{O_N:v_N\}$.

358 The variation in surface energy due to oxygen adsorption and vacancy formation on void
 359 surfaces is depicted in Fig. 6 for various porosities, oxygen concentrations, and average void
 360 radii. At low temperatures, the change in surface energy is negligible. This is because
 361 oxygen diffusivity, incorporated in the model via the kinetic correction, α_i , is very slow at
 362 low temperatures. Within the void nucleation time, the mobility of oxygen impurities is
 363 insufficient for them to reach the void surfaces. For the reference case of $w_O = 1500$ ppm,
 364 $p = 5\%$, $R_v = 1$ nm (Fig. 6b), the surface energy change is most significant at intermediate
 365 temperatures, around 1500 K, where breakaway swelling in UN is predicted to start [5].

366 The oxygen effect on stabilizing voids is more significant at intermediate temperatures
 367 due to the balance between oxygen solubility and kinetics. At very high temperatures, the
 368 increased oxygen solubility in the bulk results in a preference for oxygen to remain in the
 369 bulk rather than adsorb onto the void surfaces. The temperature that corresponds to the
 370 maximum surface energy reduction is the same for each stoichiometric condition, independent

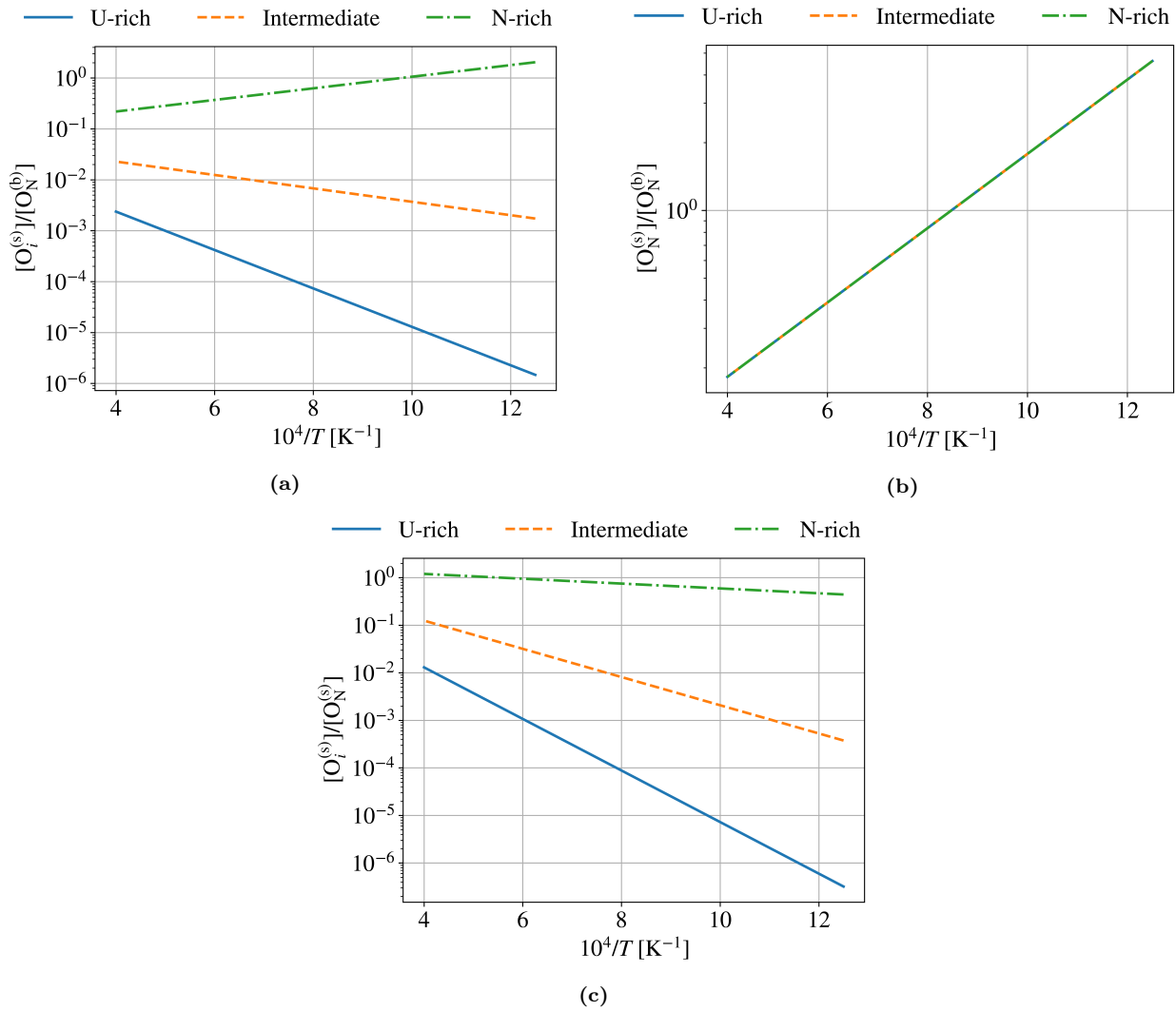


Figure 4: Relative concentrations of (a) $O_i^{(s)}$ and (b) $O_N^{(s)}$, as well as (c) the ratio of their concentrations.

of porosity and oxygen concentration (Figs. 6a to 6c). This stems from the fact that the kinetic factors, α_i , have no dependence on either porosity or oxygen concentration. The kinetic factors, however, depend on the average pore radius, i.e., $\alpha_i \sim 1/\lambda_v \sim 1/R_v$. As shown in Figs. 6b and 6d, increasing R_v from 1 nm to 10 nm shifts the temperature of maximum surface energy reduction by about 200 K to the right, and slightly decreases the overall magnitude of $\Delta\sigma$. This indicates that larger voids require higher temperatures for oxygen adsorption to meaningfully lower their surface energy. Nevertheless, even at elevated temperatures, the reduction in surface energy for larger voids remains smaller than that for smaller voids at the same porosity and oxygen concentration. Thus, oxygen-induced surface stabilization is most effective for small cavities, i.e., during the early stages of void nucleation and bubble growth.

It is of interest to examine the contribution of the different terms to the change in surface energy, where $\Delta\sigma(O_N^{(s)})$ (Eq. (33)) represents the contribution of $O_N^{(s)}$ to $\Delta\sigma$, with analogous definitions for $\Delta\sigma(O_i^{(s)})$ (Eq. (34)) and $\Delta\sigma(v_N^{(s)})$ (Eq. (35)).

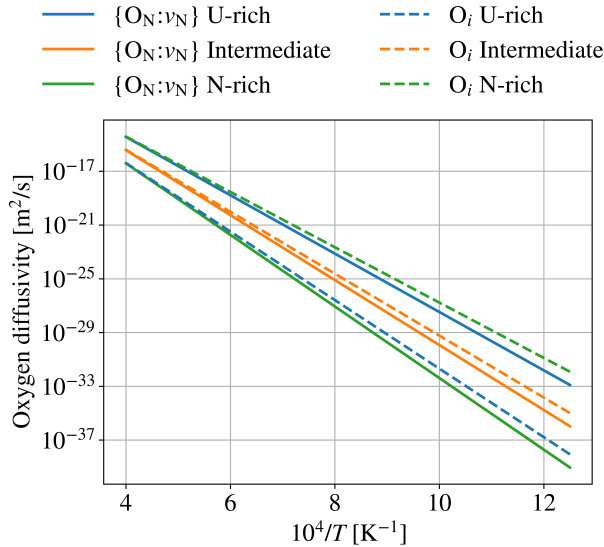


Figure 5: (Color online) Diffusivity of oxygen impurities in bulk UN by the defects $\{O_N:v_N\}$ and O_i under U-rich (blue), Intermediate (orange), and N-rich (green) conditions.

$$\Delta\sigma(O_N^{(s)}) = \frac{8}{3} \frac{1-p}{p} \frac{R_v}{a^3} c_O \alpha_1 \frac{[O_N^{(s)}]}{[O_N^{(b)}]} E_{ad}(O_N^{(s)}). \quad (33)$$

$$\Delta\sigma(O_i^{(s)}) = \frac{8}{3} \frac{1-p}{p} \frac{R_v}{a^3} c_O \alpha_2 \frac{[O_i^{(s)}]}{[O_N^{(b)}]} E_{ad}(O_i^{(s)}). \quad (34)$$

$$\Delta\sigma(v_N^{(s)}) = \frac{2}{a^2} [v_N^{(s)}] E_f(v_N^{(s)}). \quad (35)$$

These terms are plotted in Fig. 7. Comparing Figs. 6 and 7a, it can be seen that the adsorption of oxygen as $O_N^{(s)}$ dominates the $\Delta\sigma$ profile. This is expected since $O_N^{(s)}$ is the most dominant oxygen adsorption site (refer to Fig. 4c) and it leads to a reduction of surface energy at all temperatures (also see Fig. 2a). From Fig. 7b, it can be observed that $O_i^{(s)}$ is responsible for the slight surface energy increase in the range of 1020–1520 K in the N-rich profile of Fig. 6. Finally, in Fig. 7c, it is obvious that the formation of N vacancies has a negligible contribution to the surface energy change of voids.

Given that the effect of nitrogen vacancies on surface energy reduction is negligible, and the contribution of $O_i^{(s)}$ is second order, the $\Delta\sigma$ formula (Eq. (7)) simplifies to a product of four terms: a geometric factor $\eta = ((1-p)/p) \cdot R_v/3$, the oxygen number density $n_O = c_O/\Omega$, a kinetic correction factor α_1 , and an effective segregation energy $E_{seg}^{eff} = ([O_N^{(s)}]/[O_N^{(b)}]) E_{ad}(O_N^{(s)})$. Specifically, we write:

$$\Delta\sigma \approx \left(\frac{(1-p)}{p} \frac{R_v}{3} \right) \cdot \frac{c_O}{\Omega} \cdot \alpha_1 \cdot \left(\frac{[O_N^{(s)}]}{[O_N^{(b)}]} E_{ad}(O_N^{(s)}) \right) = \eta n_O \alpha_1 E_{seg}^{eff}, \quad (36)$$

where c_O is the atomic fraction of oxygen, $\Omega = a^3/8$ is the atomic volume of the matrix (inverse of the atomic number density), p is the porosity, and R_v is the average void radius.

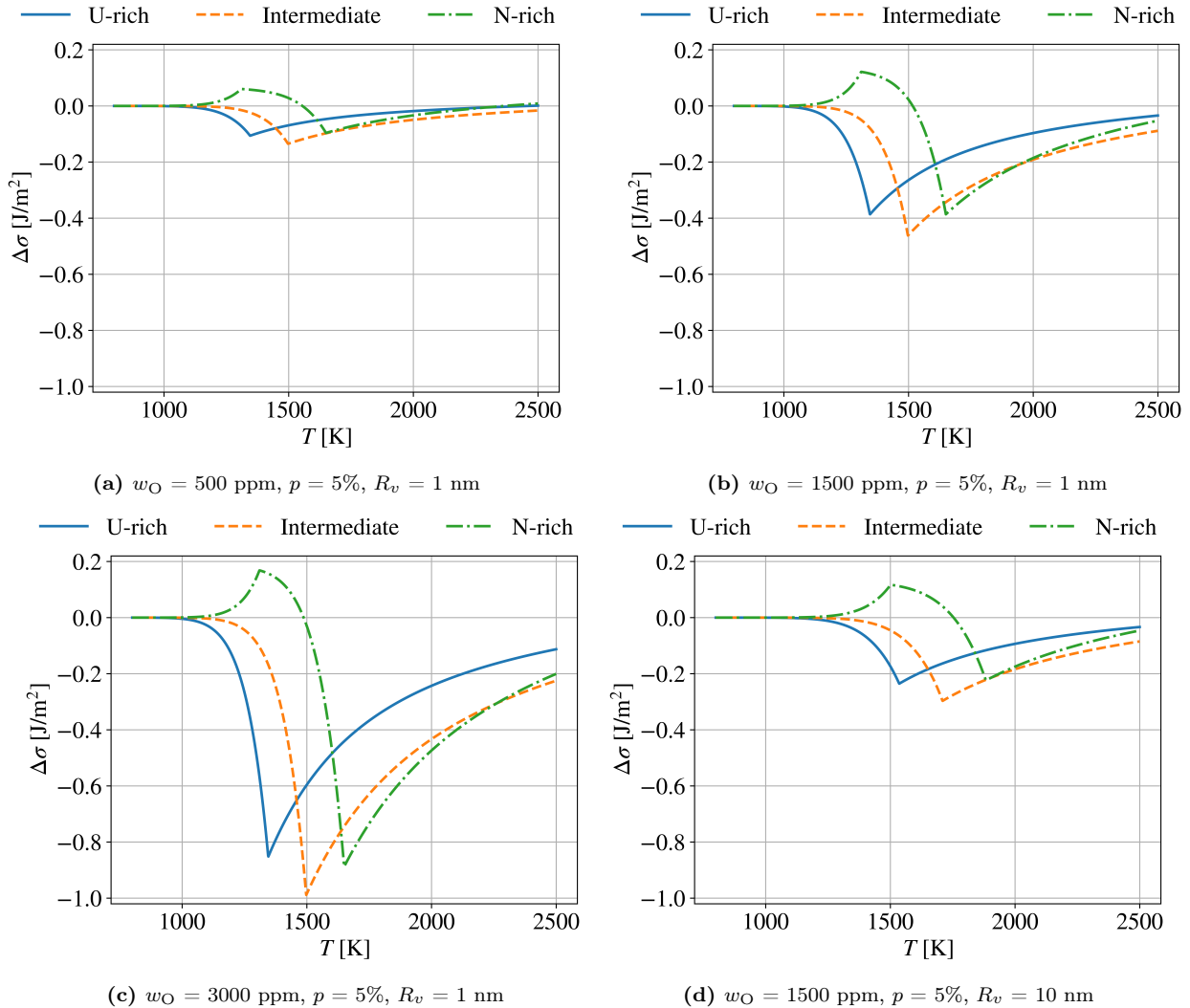


Figure 6: Temperature evolution of surface energy change due to oxygen adsorption and vacancy formation for various porosities, oxygen concentrations, and average void radii.

399 The geometric factor η captures the matrix-to-void volume ratio, $(1 - p)/p$, and the void
 400 volume-to-surface ratio, $R_v/3$. That is, η represents the average matrix volume per unit
 401 void surface area: $(V_{\text{matrix}}/V_{\text{void}}) \times (V_{\text{void}}/A_{\text{void}}) = V_{\text{matrix}}/A_{\text{void}}$, and gives a length scale that
 402 quantifies an effective thickness of matrix material supplying each unit of void surface. The
 403 kinetic correction factor α_1 accounts for the finite diffusivity of oxygen within the void nu-
 404 cleation timescale (refer to Eq. (8)). Finally, $E_{\text{seg}}^{\text{eff}}$ represents the net energy gain per oxygen
 405 atom that segregates to the void surface. This formulation makes explicit that the surface
 406 energy reduction is governed by the interplay of thermodynamics, kinetics, and microstruc-
 407 tural geometry, and scales linearly with the number of oxygen atoms that successfully reach
 408 and adsorb on the available void surface area. Note that the temperature dependence of
 409 $|\Delta\sigma|$ is contained in the anti-Arrhenius term $[O_N^{(s)}]/[O_N^{(b)}]$ and $\alpha_1 \sim \sqrt{D_1}$.

410 For the reference case of $w_O = 1500$ ppm, $p = 5\%$, and $R_v = 1$ nm, $|\Delta\sigma|$ is found to be
 411 around 0.4 J/m², occurring within the temperature interval 1300–1700 K (see Fig. 6b). To

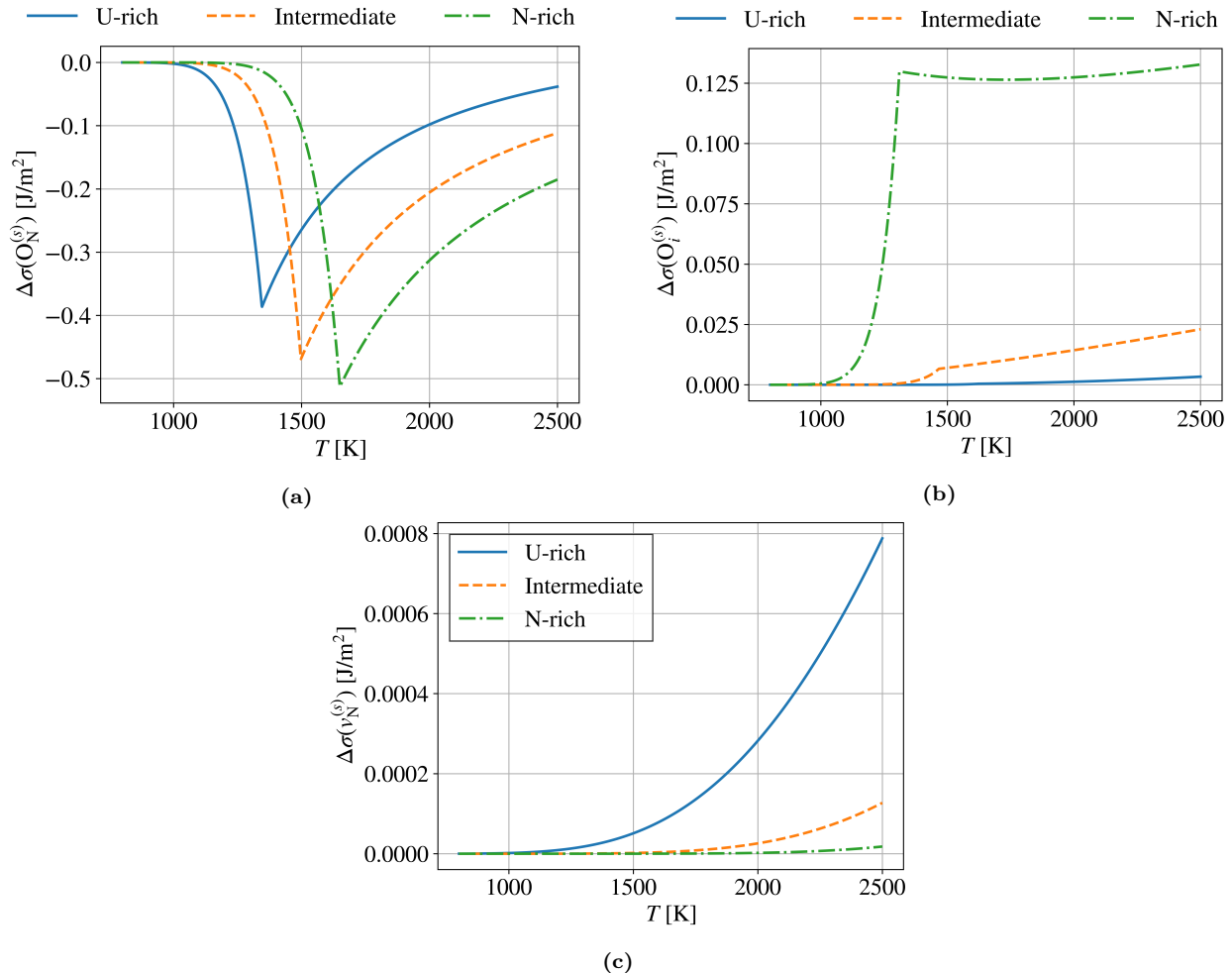


Figure 7: Different terms of the surface energy change due to oxygen adsorption and vacancy formation on void surfaces for $w_O = 1500$ ppm, $p = 5\%$, and $R_v = 1$ nm. (a) $\Delta\sigma(O_N^{(s)})$, (b) $\Delta\sigma(O_i^{(s)})$, and (c) $\Delta\sigma(v_N^{(s)})$ are given in Eqs. (33) to (35), respectively.

assess the sensitivity of $|\Delta\sigma|$ to key parameters, we vary w_O and p while holding R_v fixed at 25 nm, which is a typical size for both dislocations and intergranular bubbles [58]. It has been shown that dislocation bubbles dominate bubble swelling in UN [5–7]. Although the assumptions of our methodology are more representative of bulk voids, we assume that the same surface energy reduction mechanism applies to intragranular (bulk and dislocation) and intergranular bubbles.

Figure 8 represents the maximum $|\Delta\sigma|$, which occurs at intermediate stoichiometric conditions. As explained earlier, because R_v is kept fixed, the temperature at which this maximum occurs is the same (1800 K in the case of $R_v = 25$ nm), independent of w_O or p . The color map reveals that $|\Delta\sigma|$ is nearly independent of porosity. The vertical red line marks the oxygen concentration in UN samples from Ronchi *et al.* ($w_O = 1800$ ppm) [6, 7], used by Rizk *et al.* [5] to validate their swelling model. Fission gas bubbles with an average radius of 25 nm are predicted to experience a reduction in surface energy of about 0.3–0.4 J/m^2 , approximately 20% of our calculated surface energy in the oxygen-free case.

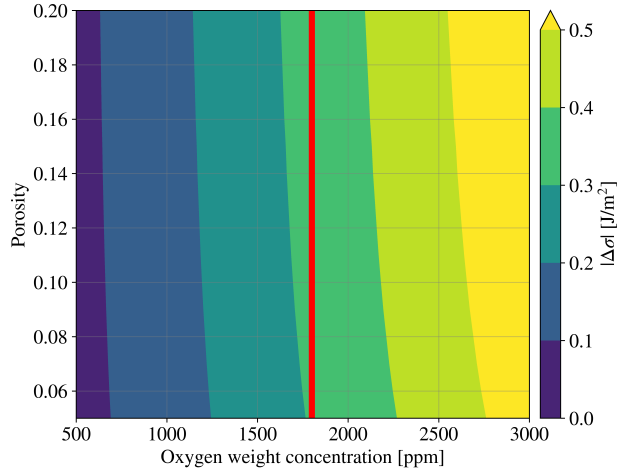


Figure 8: (Color online) Maximum surface energy reduction, $|\Delta\sigma|$ as a function of porosity and oxygen concentration under intermediate stoichiometry for a fixed bubble radius $R_v = 25$ nm, typical of dislocation and grain-boundary bubbles. The red line marks $w_O = 1800$ ppm, the oxygen concentration in UN samples from Ronchi *et al.* [6, 7], used by Rizk *et al.* [5] to validate their swelling model. Because R_v is constant, all maxima in $|\Delta\sigma|$ occur at the same temperature.

In UN samples with an oxygen content of 1600 ppm and carbon content of 300 ppm, Mishchenko *et al.* [26] found 1.5 wt.% UO₂. Thus, having an oxygen content of, e.g., 1800 ppm will most likely lead to the separation of a UO₂ phase, unless there is some process by which this oxygen is forced to be in solution. There are many solubility limits of oxygen in UN reported in the literature, ranging from 650 ppm to 6640 ppm [59–62]. Lyubimov *et al.* [25] conducted a thermodynamic modeling calculation and found that a carbon concentration of 720 ppm increases the oxygen solubility by a factor of 4–5. Based on this analysis, a carbon content of 720 ppm is large enough to keep an oxygen concentration of 3000 ppm in solution and suppress UO₂ phase separation, thus leading to $|\Delta\sigma| > 0.5$ J/m² (see Fig. 8) and enhanced void swelling in UN.

4. Discussion

This study presents a novel model that integrates first-principles calculations with defect chemistry to quantify the role of oxygen impurities in stabilizing voids and fission gas bubbles in UN. To our knowledge, this is the first model to establish a quantitative link between oxygen concentration and void nucleation thermodynamics in UN. By capturing how oxygen segregates to void surfaces and reduces the surface energy, this work advances the mechanistic understanding of swelling phenomena in oxygen-contaminated nuclear fuels. Importantly, this surface energy reduction is found to be most pronounced for void embryos ($R_v = 1$ nm) at intermediate temperatures (1300–1700 K), aligning with the temperature range associated with the onset of breakaway swelling in UN [5–7]. Noting that the range of operating temperatures in liquid metal-cooled fast reactors is 800–2000 K [54], these findings highlight oxygen adsorption as a critical factor in facilitating void nucleation under conditions typical of reactor environments.

The model provides predictive capabilities by mapping the dependence of surface en-

450 ergy reduction on key physical parameters, including temperature, porosity, void radius, and
451 oxygen concentration. Parametric analysis reveals that surface energy reduction is strongly
452 influenced by oxygen concentration and void radius, while being nearly independent of poros-
453 ity. In particular, small bulk voids and bubbles experience a significant stabilization effect
454 from oxygen at intermediate temperatures, highlighting the role of oxygen in the early stages
455 of void or fission gas bubble formation. These insights may provide a physically grounded
456 explanation for the association between oxygen content and accelerated swelling observed in
457 experimental studies of mixed uranium carbide/nitride fuels [8]. Furthermore, the general-
458 ity of the approach allows for its extension to other materials systems and integration into
459 mesoscale models and fuel performance codes, offering a path toward multiscale modeling of
460 chemically assisted swelling in nuclear materials.

461 Rizk *et al.* adopted a surface energy of 1.11 J/m^2 , computed using the empirical potential
462 developed by Kocevski *et al.* [50]. In contrast, our DFT calculations yield a higher value of
463 1.59 J/m^2 for a planar surface. This 0.48 J/m^2 discrepancy, neglecting curvature corrections,
464 likely stems from the known tendency of the Kocevski potential to underestimate defect
465 energetics in UN [38], a limitation that appears to manifest here as well. Substituting $\sigma =$
466 1.59 J/m^2 into the model of Rizk *et al.* would suppress both fission gas swelling and release,
467 necessitating recalibration of other model parameters to preserve agreement with experiment.
468 This discrepancy highlights the need for a mechanism that lowers surface energy in irradiated
469 UN. We propose that oxygen adsorption at bubble surfaces fulfills this role, enabling the
470 levels of swelling and gas release observed experimentally. A reduction in surface energy
471 thus appears essential to reconcile the mechanistic model with experimental data. Notably,
472 the oxygen concentration reported by Ronchi *et al.* ($w_O = 1800 \text{ ppm}$) corresponds to a
473 predicted surface energy reduction of $0.3\text{--}0.4 \text{ J/m}^2$, closely matching the gap between our
474 DFT value and that used by Rizk *et al.*.

475 Despite its contributions, the present model includes several simplifications that merit
476 further investigation. First, the surface adsorption energy of oxygen is assumed to be in-
477 dependent of surface coverage, which may not hold at high impurity concentrations where
478 impurity-impurity interactions become significant. Additionally, configurational and vibra-
479 tional entropy contributions are neglected, which may affect the temperature dependence
480 of defect formation and migration energies, particularly at elevated temperatures. Further,
481 the kinetic parameter used to model oxygen segregation is introduced in an *ad hoc* manner,
482 limiting the model's capability to capture time-dependent or rate-limited processes. Finally,
483 the influence of sinks such as grain boundaries and second-phase precipitates, which may
484 trap oxygen or alter defect transport, is also not incorporated.

485 A further limitation is that the current model isolates oxygen as the sole impurity species.
486 In reality, fission products and other impurities, such as carbon, krypton, and xenon, may
487 co-segregate or interact with oxygen, altering the energetics and morphology of vacancy
488 clusters. Notably, our calculations indicate that substitutional oxygen on nitrogen sites
489 binds to uranium-site vacancies and noble gas atoms (i.e., Kr_U , Xe_U) with energies around
490 -0.4 eV . Whether this binding promotes the stabilization of voids or instead alters gas
491 mobility and clustering behavior is not yet fully understood. Future studies should assess
492 how such interactions affect oxygen-assisted swelling in fission environments.

493 Finally, while the role of carbon in increasing oxygen solubility and suppressing UO_2
494 precipitation in UN is qualitatively known, the impact of carbon content on void stabilization

495 was not explicitly addressed in this model. Given that carbon can modulate the chemical
 496 potential of oxygen and influence its incorporation and redistribution, a natural extension
 497 of this work is to explore the combined effects of carbon and oxygen on defect energetics
 498 and swelling behavior in UN. The framework developed here is directly applicable to this
 499 scenario.

500 5. Conclusions

501 This work develops a first-principles-based thermodynamic framework that quantifies how
 502 oxygen impurities interact with void surfaces in UN, leading to a reduction in the surface
 503 energy, $|\Delta\sigma|$. The model incorporates DFT-derived energetics, oxygen diffusivity, defect
 504 chemistry, and microstructural parameters to assess the extent of surface stabilization.

505 Key findings can be summarized as follows. Substitutional oxygen on nitrogen surface
 506 sites ($O_N^{(s)}$) is the dominant contributor to surface energy reduction. Oxygen in surface hollow
 507 sites ($O_i^{(s)}$) has a minor, and occasionally adverse, effect on $|\Delta\sigma|$. The dependence of $|\Delta\sigma|$
 508 on key parameters is summarized below:

- 509 • *Oxygen concentration (w_O):* The surface energy reduction scales linearly with oxygen
 510 content.
- 511 • *Void radius (R_v):* $|\Delta\sigma|$ is most pronounced for small voids. Larger voids require higher
 512 temperatures to reach meaningful oxygen coverage and experience a slightly smaller
 513 $|\Delta\sigma|$.
- 514 • *Porosity (p):* The surface energy reduction is found to be largely insensitive to porosity.

515 For small voids and bubbles ($R_v = 1\text{--}10 \text{ nm}$), $|\Delta\sigma|$ exhibits three regimes in its depen-
 516 dence on temperature:

- 517 • *Low temperatures:* $|\Delta\sigma| \approx 0$ due to limited oxygen diffusivity.
- 518 • *Intermediate temperatures:* $|\Delta\sigma|$ reaches its maximum as the competing effects of
 519 oxygen solubility and diffusion kinetics are optimally balanced. This regime coincides
 520 with the onset of breakaway swelling in UN.
- 521 • *High temperatures:* $|\Delta\sigma|$ decreases due to enhanced bulk solubility, which disfavors
 522 surface segregation.

523 The reduction in surface energy can be approximately expressed as:

$$|\Delta\sigma| \approx \eta n_O \alpha_1 |E_{\text{seg}}^{\text{eff}}|,$$

524 where η is a geometric factor that depends on p and R_v , n_O is the oxygen number density,
 525 α_1 is a kinetic correction factor, and $E_{\text{seg}}^{\text{eff}}$ is the effective segregation energy. The reduction
 526 in σ lowers the thermodynamic barrier for void and bubble formation. For the reference case
 527 of $w_O = 1800 \text{ ppm}$ in UN [6], our model predicts a surface energy reduction of about 0.3–0.4
 528 J/m^2 for dislocation and grain-boundary bubbles. This aligns closely with the discrepancy
 529 between our DFT-calculated surface energy (1.59 J/m^2) and the value adopted by Rizk *et*
 530 *al.* [5] in their swelling model (1.11 J/m^2). The oxygen-induced reduction in σ thus can offer
 531 a mechanistic explanation for the experimentally observed levels of swelling and fission gas
 532 release in UN.

Overall, this work provides a physically rigorous model for incorporating oxygen effects into mechanistic swelling models of UN. The framework is extendable to other chemical impurities such as carbon and can be integrated into mesoscale and fuel performance models to predict chemically-assisted bubble swelling in nuclear fuels.

6. Acknowledgments

This work was supported by the DOE-NE and Westinghouse Electric Company under contract DE-NE0008824. This research used resources provided by the Los Alamos National Laboratory Institutional Computing Program, which is supported by the U.S. Department of Energy National Nuclear Security Administration under Contract No. 89233218CNA000001. Los Alamos National Laboratory, an affirmative action/equal opportunity employer, is operated by Triad National Security, LLC, for the National Nuclear Security Administration of the U.S. Department of Energy under Contract No. 89233218CNA000001. This research also made use of the resources of the High-Performance Computing Center at Idaho National Laboratory, which is supported by the Office of Nuclear Energy of the U.S. Department of Energy and the Nuclear Science User Facilities under Contract No. DE-AC07-05ID14517. Mohamed AbdulHameed thanks William Neilson, Conor Galvin, and Kai Duemmler for the great help provided while conducting this research.

Appendix A. Derivation of the formulas for $[N_N^{(s)}]$ and $[v_i^{(s)}]$

The area associated with an N atom on the surface is $a^2/2$, where a is the lattice constant. The total surface area of the internal voids is $N_v \times 4\pi R_v^2$, where N_v is the total number of voids, calculated as:

$$N_v = \frac{pV_0}{\frac{4}{3}\pi R_v^3}, \quad (\text{A.1})$$

where V_0 is the total system volume. Then, the number of $N_N^{(s)}$ sites is:

$$\text{Number of } N_N^{(s)} = \frac{N_v \times 4\pi R_v^2}{a^2/2}. \quad (\text{A.2})$$

To get the site fraction of $N_N^{(s)}$, we need to divide its total number by the number of formula units. The number of formula units is:

$$\text{Number of formula units} = \frac{V_0(1-p)}{a^3/4}, \quad (\text{A.3})$$

where $V_0(1-p)$ is the occupied volume, and $a^3/4$ is the volume of a single formula unit. Dividing Eq. (A.2) by Eq. (A.3), we arrive at:

$$[N_N^{(s)}] = \frac{pV_0}{\frac{4}{3}\pi R_v^3} \frac{4\pi R_v^2}{a^2/2} \frac{a^3/4}{V_0(1-p)} = \frac{3}{2} \frac{p}{1-p} \frac{a}{R_v}. \quad (\text{A.4})$$

559 The same steps can be followed to get an expression for $[v_i^{(s)}]$, provided that we pay
 560 attention to the following differences: First, the area occupied by a vacant site on the surface
 561 is $a^2/4$. Then, the number of $v_i^{(s)}$ sites is:

$$\text{Number of } v_i^{(s)} = \frac{N_v \times 4\pi R_v^2}{a^2/4}. \quad (\text{A.5})$$

562 To get the site fraction of $v_i^{(s)}$, we need to divide its total number by the number of formula
 563 units in the occupied volume (i.e., Eq. (A.3)), and then divide by 2 because there are 2
 564 tetrahedral interstitial sites per formula unit, either in the bulk material or on the surface.
 565 In the case of $[N_N^{(s)}]$, there was one N atom (or site) per formula unit. Then, the site fraction
 566 of $v_i^{(s)}$ is:

$$[v_i^{(s)}] = \frac{1}{2} \frac{pV_0}{\frac{4}{3}\pi R_v^3} \frac{4\pi R_v^2}{a^2/4} \frac{a^3/4}{V_0(1-p)} = \frac{3}{2} \frac{p}{1-p} \frac{a}{R_v}, \quad (\text{A.6})$$

567 which is the same expression for $[N_N^{(s)}]$. Note that both Eqs. (A.4) and (A.6) are independent
 568 of V_0 . As outlined in Section 3.1, the adsorption energy of O atoms in above-U sites is the
 569 same as that of O in a hollow site (Table 6). To account for this in our model, the available
 570 adsorption sites are doubled by multiplying $[v_i^{(s)}]$ by 2. In this way, the analysis is simplified
 571 by only considering $O_i^{(s)}$. The final expression reads:

$$[v_i^{(s)}] = \frac{3p}{1-p} \frac{a}{R_v}. \quad (\text{A.7})$$

572 Appendix B. Derivation of the formula for surface energy change as a function 573 of adsorbate atom concentration

574 Suppose we have an impurity atom that got adsorbed on a pristine surface. The surface
 575 energy after absorption is:

$$\sigma = \sigma_0 + \Delta\sigma, \quad (\text{B.1})$$

576 where σ_0 is the energy of the pristine surface before adsorption, and $\Delta\sigma$ is the surface energy
 577 change due to impurity adsorption. The change in the surface energy can be expressed as:

$$\Delta\sigma = \sigma_{\text{surf+ad}} - \sigma_{\text{surf}}, \quad (\text{B.2})$$

578 where:

$$\sigma_{\text{surf}} = \frac{1}{A} [E_{\text{surf}} - N_U \mu_U - N_N \mu_N], \quad (\text{B.3})$$

579 and:

$$\sigma_{\text{surf+ad}} = \frac{1}{A} [E_{\text{surf+ad}} - N_U \mu_U - N_N \mu_N - N_{\text{ad}} \mu_{\text{ad}}]. \quad (\text{B.4})$$

580 Then,

$$\Delta\sigma = \frac{1}{A} [E_{\text{surf+ad}} - E_{\text{surf}} - N_{\text{ad}} \mu_{\text{ad}}]. \quad (\text{B.5})$$

581 From the definition of the adsorption energy, i.e., Eq. (6), the change in the surface energy
 582 is:

$$\Delta\sigma = \frac{1}{A} [N_{\text{ad}} (E_{\text{ad}} + \mu_{\text{ad}}) - N_{\text{ad}} \mu_{\text{ad}}] = \frac{1}{A} N_{\text{ad}} E_{\text{ad}}. \quad (\text{B.6})$$

583 If we have a specific concentration of an impurity that can get adsorbed on different sites
 584 on the surface, with each site type having its own adsorption energy, then:

$$\Delta\sigma = \frac{1}{A} \left[\sum_i N_{\text{ad}}^i E_{\text{ad}}^i \right]. \quad (\text{B.7})$$

585 The same line of thought can be used to derive an expression for the surface energy change
 586 upon introducing vacancies to a previously pristine surface. For the general case where we
 587 introduce both adsorbate atoms and vacancies to a surface, the total surface energy change
 588 is:

$$\Delta\sigma = \frac{1}{A} \left[\sum_i N_{\text{ad}}^i E_{\text{ad}}^i + \sum_j N_d^j E_f^j \right]. \quad (\text{B.8})$$

589 This can be related to the relative concentrations calculated earlier by noticing that:

$$N_{\text{ad}}^i = N_O \frac{N_{\text{ad}}^i}{N_O} \approx N_O \frac{[\text{O}_X^{(\text{s})}]}{[\text{O}_N^{(\text{b})}]}, \quad (\text{B.9})$$

590 where N_O is the total number of oxygen atoms in the sample and $X \in \{\text{N}, i\}$. Finally, we can
 591 relate N_d , i.e., the total number of surface defects, to the concentrations calculated earlier
 592 by a similar argument. Assuming the surface defect is $v_N^{(\text{s})}$, we have:

$$N_d = [v_N^{(\text{s})}] \times \text{Number of } \text{N}_N^{(\text{s})} = [v_N^{(\text{s})}] \frac{A_v}{a^2/2}, \quad (\text{B.10})$$

593 where we have made use of Eq. (A.2) with A_v being the total area of the void surface.

594 The total number of oxygen atoms in the system is not a useful parameter. Instead, we
 595 need the formulas to be expressed in terms of some measure of oxygen concentration. The
 596 number of voids is expressed in terms of both the void surface area and the void volume as:

$$N_v = \frac{A_v}{4\pi R_v^2} = \frac{pV_0}{\frac{4}{3}\pi R_v^3}. \quad (\text{B.11})$$

597 From Eq. (B.11), the total void surface area is:

$$A_v = \frac{3pV_0}{R_v} = \frac{3}{R_v} \frac{p}{1-p} V. \quad (\text{B.12})$$

598 Then,

$$\frac{N_O}{A_v} = \frac{R_v}{3} \frac{1-p}{p} \frac{N_O}{V} = \frac{R_v}{3} \frac{1-p}{p} \frac{N_O}{2N_{\text{UN}} \cdot a^3/8} \approx \frac{8}{3} \frac{1-p}{p} \frac{R_v}{a^3} c_O, \quad (\text{B.13})$$

599 where N_{UN} is the number of formula units in the occupied volume, $a^3/8$ is the average
 600 volume per atom of UN, and c_O is the atomic fraction of O atoms which is approximately
 601 $c_O \approx N_O/(2N_{\text{UN}})$. The oxygen impurity concentration in UN is usually expressed as parts
 602 per million (ppm) or weight fractions. The relation between atomic fraction, c_O , and weight
 603 fraction, w_O , is:

$$c_O = \frac{M_{\text{UN}} w_O}{M_{\text{UN}} w_O + 2M_O(1 - w_O)}, \quad (\text{B.14})$$

604 where M_{UN} and M_{O} are the molar weights of UN and O, respectively. From Eq. (B.14), w_{O}
 605 can be expressed in terms of c_{O} as:

$$w_{\text{O}} = \frac{2M_{\text{O}}c_{\text{O}}}{2M_{\text{O}}c_{\text{O}} + M_{\text{UN}}(1 - c_{\text{O}})}. \quad (\text{B.15})$$

606 Substituting Eqs. (B.9), (B.10) and (B.13) into Eq. (B.8), the change in surface energy
 607 becomes:

$$\Delta\sigma = \frac{8}{3} \frac{1-p}{p} \frac{R_v}{a^3} c_{\text{O}} \left[\frac{[\text{O}_N^{(\text{s})}]}{[\text{O}_N^{(\text{b})}]} E_{\text{ad}}(\text{O}_N^{(\text{s})}) + \frac{[\text{O}_i^{(\text{s})}]}{[\text{O}_N^{(\text{b})}]} E_{\text{ad}}(\text{O}_i^{(\text{s})}) \right] + \frac{2}{a^2} [v_N^{(\text{s})}] E_f(v_N^{(\text{s})}). \quad (\text{B.16})$$

608 To take kinetics into account, the concentrations of the different oxygen surface defects
 609 must be corrected for the low oxygen diffusivity at low temperatures. Note that the increased
 610 oxygen solubility is inherently incorporated in the thermodynamic model. According to
 611 Zinkle and Lee [12], as a first approximation, the concentrations of oxygen surface defects
 612 can be multiplied by a parameter α that we term the kinetic correction, and that depends
 613 on the diffusivity of different oxygen defect types. Thus, the final expression for the change
 614 in surface energy becomes:

$$\Delta\sigma = \frac{8}{3} \frac{1-p}{p} \frac{R_v}{a^3} c_{\text{O}} \left[\alpha_1 \frac{[\text{O}_N^{(\text{s})}]}{[\text{O}_N^{(\text{b})}]} E_{\text{ad}}(\text{O}_N^{(\text{s})}) + \alpha_2 \frac{[\text{O}_i^{(\text{s})}]}{[\text{O}_N^{(\text{b})}]} E_{\text{ad}}(\text{O}_i^{(\text{s})}) \right] + \frac{2}{a^2} [v_N^{(\text{s})}] E_f(v_N^{(\text{s})}), \quad (\text{B.17})$$

615 where α_1 and α_2 are the kinetic corrections for the defects $\text{O}_N^{(\text{s})}$ and $\text{O}_i^{(\text{s})}$, respectively. Con-
 616 ceptually, α_i stems from the fraction of diffusing oxygen atoms that encounter a void embryo
 617 during the void nucleation time, and, thus, can be defined as [12]:

$$\alpha_i = \begin{cases} \sqrt{D_i t} / \lambda_v & \text{if } \sqrt{D_i t} / \lambda_v < 1, \\ 1 & \text{if } \sqrt{D_i t} / \lambda_v \geq 1, \end{cases} \quad (\text{B.18})$$

618 where D_i is the diffusivity of the relevant defect, t is the void nucleation time, and λ_v is the
 619 mean free path between voids, defined as $\lambda_v = n_v^{-1/3}$ [63], where $n_v = p / (\frac{4}{3}\pi R_v^3)$ is the void
 620 number density.

621 Appendix C. Supplementary information

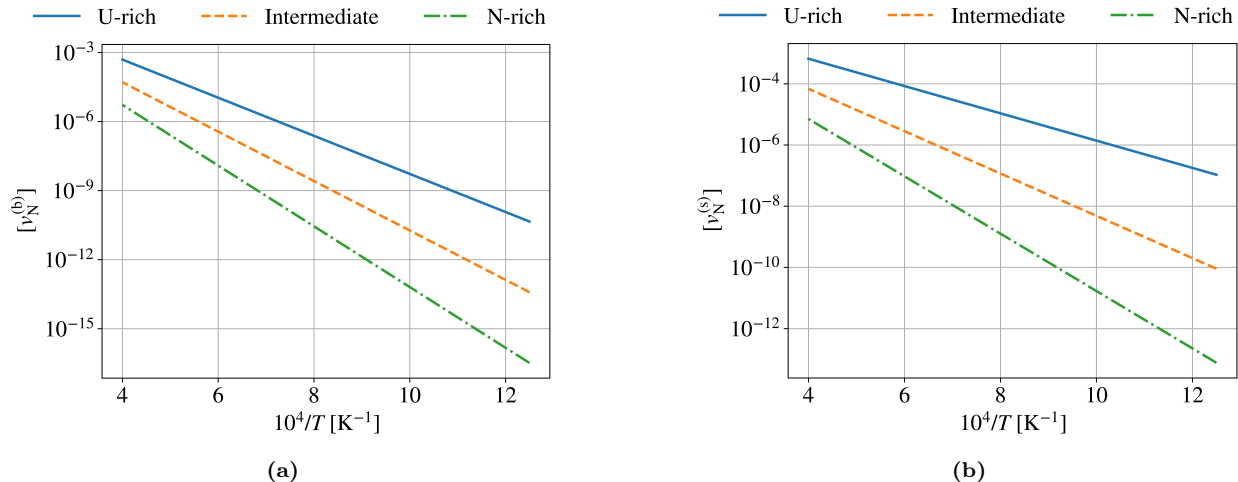


Figure C.9: (a) Concentration of N vacancies in bulk UN calculated from the formation energies in [Table 1](#). (b) Concentration of N vacancies on the UN (001) surface calculated from the formation energies in [Table 1](#).

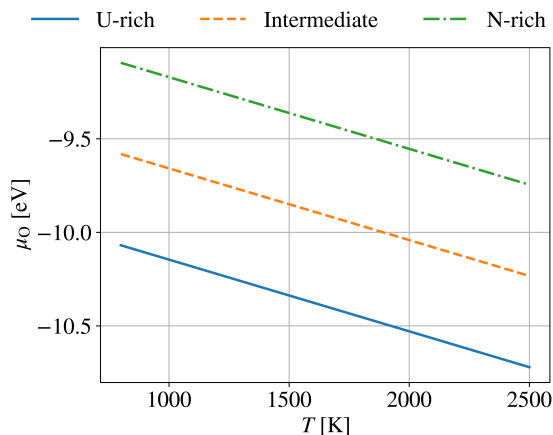


Figure C.10: Oxygen chemical potential as calculated based on Eq. (16).

622 References

- [1] J. Wallenius, Nitride fuels, *Comprehensive Nuclear Materials* 5 (2020) 88–101. doi: [10.1016/B978-0-12-803581-8.11694-7](https://doi.org/10.1016/B978-0-12-803581-8.11694-7).

[2] M. Uno, T. Nishi, M. Takano, Thermodynamic and thermophysical properties of the actinide nitrides, *Comprehensive Nuclear Materials: Second Edition* (2020) 202–231 doi: [10.1016/B978-0-12-803581-8.11749-7](https://doi.org/10.1016/B978-0-12-803581-8.11749-7).

[3] M. AbdulHameed, B. Beeler, A. Claisse, Atomistic investigation of plastic deformation and dislocation motion in uranium mononitride, *Applied Sciences* 15 (2024) 2666. doi: <https://doi.org/10.3390/app15052666>.

[4] M. AbdulHameed, B. Beeler, C. O. Galvin, M. W. Cooper, N. Elamrawy, A. Claisse, Molecular-dynamics study of diffusional creep in uranium mononitride (2025). doi: <https://doi.org/10.48550/arXiv.2503.03231>.

- [5] J. T. Rizk, M. W. Cooper, P.-C. A. Simon, A. J. Schneider, D. A. Andersson, S. R. Novascone, C. Matthews, Mechanistic nuclear fuel performance modeling of uranium nitride, *Journal of Nuclear Materials* 606 (2025) 155604. [doi:
https://doi.org/10.1016/j.jnucmat.2024.155604](https://doi.org/10.1016/j.jnucmat.2024.155604).
- [6] C. Ronchi, C. Sari, Swelling analysis of highly rated MX-type LMFBR fuels. I. Restructuring and porosity behaviour, *Journal of Nuclear Materials* 58 (1975). [doi:
10.1016/0022-3115\(75\)90100-2](https://doi.org/10.1016/0022-3115(75)90100-2).
- [7] C. Ronchi, I. L. Ray, H. Thiele, J. van de Laar, Swelling analysis of highly-rated MX-type LMFBR fuels: II. Microscopic swelling behaviour, *Journal of Nuclear Materials* 74 (1978). [doi:
10.1016/0022-3115\(78\)90359-8](https://doi.org/10.1016/0022-3115(78)90359-8).
- [8] B. D. Rogozkin, N. M. Stepennova, A. A. Proshkin, Mononitride fuel for fast reactors, *Atomic Energy* 95 (2003). [doi:
10.1023/B:ATEN.0000007886.86817.32](https://doi.org/10.1023/B:ATEN.0000007886.86817.32).
- [9] T. Schuler, D. A. Lopes, A. Claisse, P. Olsson, Transport properties of C and O in UN fuels, *Physical Review B* 95 (2017). [doi:
10.1103/PhysRevB.95.094117](https://doi.org/10.1103/PhysRevB.95.094117).
- [10] S. J. Zinkle, L. E. Seitzman, W. G. Wolfer, Stability of vacancy clusters in metals: I. energy calculations for pure metals, *Philosophical Magazine A* 55 (1987).
- [11] S. J. Zinkle, W. G. Wolfer, G. L. Kulcinski, L. E. Seitzman, Stability of vacancy clusters in metals: II. effect of oxygen and helium on void formation in metals, *Philosophical Magazine A* 55 (1987).
- [12] S. J. Zinkle, E. H. Lee, Effect of oxygen on vacancy cluster morphology in metals, *Metallurgical Transactions A* 21 (1990). [doi:
10.1007/BF02656525](https://doi.org/10.1007/BF02656525).
- [13] N. Igata, A. Ryazanov, D. N. Korolev, Effect of light impurities on the early stage of swelling in austenitic stainless steel, *Journal of Nuclear Materials* 258-263 (1998). [doi:
10.1016/S0022-3115\(98\)00404-8](https://doi.org/10.1016/S0022-3115(98)00404-8).
- [14] E. A. Kotomin, Y. A. Mastrikov, First principles modeling of oxygen impurities in UN nuclear fuels, *Journal of Nuclear Materials* 377 (2008) 492–495. [doi:
10.1016/j.jnucmat.2008.04.015](https://doi.org/10.1016/j.jnucmat.2008.04.015).
- [15] E. A. Kotomin, Y. A. Mastrikov, S. N. Rashkeev, P. V. Uffelen, Implementing first principles calculations of defect migration in a fuel performance code for UN simulations, *Journal of Nuclear Materials* 393 (2009) 292–299. [doi:
10.1016/j.jnucmat.2009.06.016](https://doi.org/10.1016/j.jnucmat.2009.06.016).
- [16] Y. F. Zhukovskii, D. Bocharov, E. A. Kotomin, Chemisorption of molecular oxygen on the UN (001) surface: Ab initio calculations, *Journal of Nuclear Materials* 393 (2009). [doi:
10.1016/j.jnucmat.2009.07.010](https://doi.org/10.1016/j.jnucmat.2009.07.010).
- [17] Y. F. Zhukovskii, D. Bocharov, E. A. Kotomin, R. A. Evarestov, A. V. Bandura, First principles calculations of oxygen adsorption on the UN (001) surface, *Surface Science* 603 (2009). [doi:
10.1016/j.susc.2008.10.019](https://doi.org/10.1016/j.susc.2008.10.019).

- 671 [18] D. Bocharov, D. Gryaznov, Y. F. Zhukovskii, E. A. Kotomin, Ab initio modeling of
672 oxygen impurity atom incorporation into uranium mononitride surface and sub-surface
673 vacancies, Journal of Nuclear Materials 416 (2011). [doi:10.1016/j.jnucmat.2010.11.090](https://doi.org/10.1016/j.jnucmat.2010.11.090).
- 675 [19] D. Bocharov, D. Gryaznov, Y. F. Zhukovskii, E. A. Kotomin, DFT calculations of point
676 defects on UN (001) surface, Surface Science 605 (2011) 396–400. [doi:10.1016/j.susc.2010.11.007](https://doi.org/10.1016/j.susc.2010.11.007).
- 678 [20] D. Bocharov, D. Gryaznov, Y. F. Zhukovskii, E. A. Kotomin, Ab initio simulations
679 of oxygen interaction with surfaces and interfaces in uranium mononitride, Journal of
680 Nuclear Materials 435 (2013). [doi:10.1016/j.jnucmat.2012.12.031](https://doi.org/10.1016/j.jnucmat.2012.12.031).
- 681 [21] D. A. Lopes, A. Claisse, P. Olsson, Ab-initio study of C and O impurities in uranium
682 nitride, Journal of Nuclear Materials 478 (2016). [doi:10.1016/j.jnucmat.2016.06.008](https://doi.org/10.1016/j.jnucmat.2016.06.008).
- 684 [22] T. Zergoug, S. E. Abaidia, A. Nedjar, Oxygen diffusion and migration in clean and
685 defective uranium nitride (UN) (001) surfaces, Computational Materials Science 144
686 (2018). [doi:10.1016/j.commatsci.2017.12.003](https://doi.org/10.1016/j.commatsci.2017.12.003).
- 687 [23] E. L. Sikorski, B. J. Jaques, L. Li, First-principles magnetic treatment of the uranium
688 nitride (100) surface and effect on corrosion initiation, Journal of Applied Physics 130
689 (2021). [doi:10.1063/5.0056904](https://doi.org/10.1063/5.0056904).
- 690 [24] V. Kocevski, D. A. Rehn, M. W. D. Cooper, D. A. Andersson, First-principles investi-
691 gation of uranium mononitride (UN): Effect of magnetic ordering, spin-orbit inter-
692 actions and exchange correlation functional, Journal of Nuclear Materials 559 (2022).
693 [doi:10.1016/j.jnucmat.2021.153401](https://doi.org/10.1016/j.jnucmat.2021.153401).
- 694 [25] D. Y. Lyubimov, A. V. Androsov, G. S. Bulatov, K. N. Gedgovd, Thermodynamic
695 modeling of oxygen dissolution in uranium mononitride at 900–1400 K, Radiochemistry
696 56 (2014). [doi:10.1134/S1066362214050087](https://doi.org/10.1134/S1066362214050087).
- 697 [26] Y. Mishchenko, K. D. Johnson, D. Jädernäs, J. Wallenius, D. A. Lopes, Uranium nitride
698 advanced fuel: an evaluation of the oxidation resistance of coated and doped grains,
699 Journal of Nuclear Materials 556 (2021). [doi:10.1016/j.jnucmat.2021.153249](https://doi.org/10.1016/j.jnucmat.2021.153249).
- 700 [27] G. Kresse, J. Hafner, Ab initio molecular dynamics for liquid metals, Physical Review
701 B 47 (1993). [doi:10.1103/PhysRevB.47.558](https://doi.org/10.1103/PhysRevB.47.558).
- 702 [28] G. Kresse, J. Furthmüller, Efficiency of ab-initio total energy calculations for metals
703 and semiconductors using a plane-wave basis set, Computational Materials Science 6
704 (1996). [doi:10.1016/0927-0256\(96\)00008-0](https://doi.org/10.1016/0927-0256(96)00008-0).
- 705 [29] G. Kresse, J. Furthmüller, Efficient iterative schemes for ab initio total-energy calcula-
706 tions using a plane-wave basis set, Physical Review B - Condensed Matter and Materials
707 Physics 54 (1996). [doi:10.1103/PhysRevB.54.11169](https://doi.org/10.1103/PhysRevB.54.11169).

- 708 [30] J. P. Perdew, K. Burke, M. Ernzerhof, Generalized gradient approximation made simple,
709 Physical Review Letters 77 (1996). [doi:10.1103/PhysRevLett.77.3865](https://doi.org/10.1103/PhysRevLett.77.3865).
- 710 [31] G. Kresse, D. Joubert, From ultrasoft pseudopotentials to the projector augmented-
711 wave method, Physical Review B - Condensed Matter and Materials Physics 59 (1999).
712 [doi:10.1103/PhysRevB.59.1758](https://doi.org/10.1103/PhysRevB.59.1758).
- 713 [32] M. Methfessel, A. T. Paxton, High-precision sampling for Brillouin-zone integration in
714 metals, Physical Review B 40 (1989). [doi:10.1103/PhysRevB.40.3616](https://doi.org/10.1103/PhysRevB.40.3616).
- 715 [33] H. J. Monkhorst, J. D. Pack, Special points for Brillouin-zone integrations, Physical
716 Review B 13 (1976). [doi:10.1103/PhysRevB.13.5188](https://doi.org/10.1103/PhysRevB.13.5188).
- 717 [34] G. Henkelman, H. Jónsson, Improved tangent estimate in the nudged elastic band
718 method for finding minimum energy paths and saddle points, Journal of Chemical
719 Physics 113 (2000). [doi:10.1063/1.1323224](https://doi.org/10.1063/1.1323224).
- 720 [35] G. Henkelman, B. P. Uberuaga, H. Jónsson, Climbing image nudged elastic band method
721 for finding saddle points and minimum energy paths, Journal of Chemical Physics 113
722 (2000). [doi:10.1063/1.1329672](https://doi.org/10.1063/1.1329672).
- 723 [36] A. Stukowski, Visualization and analysis of atomistic simulation data with OVITO—the
724 open visualization tool, Modelling and Simulation in Materials Science and Engineering
725 18 (2010). [doi:10.1088/0965-0393/18/1/015012](https://doi.org/10.1088/0965-0393/18/1/015012).
- 726 [37] K. Momma, F. Izumi, VESTA: A three-dimensional visualization system for electronic
727 and structural analysis, Journal of Applied Crystallography 41 (2008). [doi:10.1107/S0021889808012016](https://doi.org/10.1107/S0021889808012016).
- 729 [38] M. AbdulHameed, B. Beeler, C. O. Galvin, M. W. Cooper, Assessment of uranium
730 nitride interatomic potentials, Journal of Nuclear Materials (2024) 155247 [doi:https://doi.org/10.1016/j.jnucmat.2024.155247](https://doi.org/10.1016/j.jnucmat.2024.155247).
- 732 [39] G. Y. Huang, G. Pastore, B. D. Wirth, First-principles study of intrinsic point defects
733 and Xe impurities in uranium monocarbide, Journal of Applied Physics 128 (2020).
734 [doi:10.1063/5.0021951](https://doi.org/10.1063/5.0021951).
- 735 [40] L. Yang, N. Kaltsoyannis, Incorporation of Kr and Xe in uranium mononitride: A
736 density functional theory study, Journal of Physical Chemistry C 125 (2021) 26999–
737 27008. [doi:10.1021/acs.jpcc.1c08523](https://doi.org/10.1021/acs.jpcc.1c08523).
- 738 [41] C. Woodward, S. Kajihara, L. H. Yang, Site preferences and formation energies of
739 substitutional Si, Nb, Mo, Ta, and W solid solutions in $L1_0$ Ti-Al, Physical Review B
740 57 (1998).
- 741 [42] M. W. Finnis, A. Y. Lozovoi, A. Alavi, The oxidation of NiAl: What can we learn from
742 ab initio calculations? (2005). [doi:10.1146/annurev.matsci.35.101503.091652](https://doi.org/10.1146/annurev.matsci.35.101503.091652).

- 743 [43] L. K. Mansur, W. A. Coghlani, Mechanisms of helium interaction with radiation effects
744 in metals and alloys: A review, Journal of Nuclear Materials 119 (1983). [doi:10.1016/0022-3115\(83\)90047-8](https://doi.org/10.1016/0022-3115(83)90047-8).
- 745
- 746 [44] U. Saha, K. Devan, A. Bachchan, G. Pandikumar, S. Ganesan, Neutron radiation
747 damage studies in the structural materials of a 500 MWe fast breeder reactor using
748 DPA cross-sections from ENDF/B-VII.1, Pramana - Journal of Physics 90 (2018).
749 [doi:10.1007/s12043-018-1536-y](https://doi.org/10.1007/s12043-018-1536-y).
- 750 [45] M. Surh, J. Sturgeon, W. Wolfer, Incubation period for void swelling and its dependence
751 on temperature, dose rate, and dislocation structure evolution, in: Effects of Radiation
752 on Materials: 21st International Symposium, ASTM International, 2004. [doi:10.1520/STP11245S](https://doi.org/10.1520/STP11245S).
- 753
- 754 [46] E. Sargeant, F. Illas, P. Rodríguez, F. Calle-Vallejo, Importance of the gas-phase error
755 correction for O₂ when using DFT to model the oxygen reduction and evolution reac-
756 tions, Journal of Electroanalytical Chemistry 896 (2021). [doi:10.1016/j.jelechem.2021.115178](https://doi.org/10.1016/j.jelechem.2021.115178).
- 757
- 758 [47] P. J. Linstrom, W. G. Mallard, [NIST Chemistry WebBook](#), NIST Standard Reference
759 Database Number 69, National Institute of Standards and Technology, 2024. [doi:10.18434/T4D303](https://doi.org/10.18434/T4D303).
760
- 761 URL <https://doi.org/10.18434/T4D303>
- 762 [48] F. A. Kröger, H. J. Vink, Relations between the concentrations of imperfections in
763 crystalline solids, Solid State Physics - Advances in Research and Applications 3 (1956).
764 [doi:10.1016/S0081-1947\(08\)60135-6](https://doi.org/10.1016/S0081-1947(08)60135-6).
- 765
- 766 [49] M. W. Cooper, J. Rizk, C. Matthews, V. Kocevski, G. T. Craven, T. Gibson, D. A.
767 Andersson, Simulations of self- and Xe diffusivity in uranium mononitride including
768 chemistry and irradiation effects, Journal of Nuclear Materials 587 (2023). [doi:10.1016/j.jnucmat.2023.154685](https://doi.org/10.1016/j.jnucmat.2023.154685).
- 769
- 770 [50] V. Kocevski, M. W. Cooper, A. J. Claisse, D. A. Andersson, Development and appli-
771 cation of a uranium mononitride (UN) potential: Thermomechanical properties and
772 Xe diffusion, Journal of Nuclear Materials 562 (2022). [doi:10.1016/j.jnucmat.2022.153553](https://doi.org/10.1016/j.jnucmat.2022.153553).
- 773
- 774 [51] A. Claisse, T. Schuler, D. A. Lopes, P. Olsson, Transport properties in dilute UN(X)
775 solid solutions (X = Xe, Kr), Physical Review B 94 (2016). [doi:10.1103/PhysRevB.94.174302](https://doi.org/10.1103/PhysRevB.94.174302).
- 776
- 777 [52] D. R. Olander, A. T. Motta, Light Water Reactor Materials Volume I: Fundamentals,
American Nuclear Society, 2017.
- 778
- 779 [53] D. E. Laughlin, K. Hono (Eds.), Physical Metallurgy, 5th Edition, Vol. 1, Elsevier, 2014.
- 780
- [54] A. Turos, S. Fritz, H. Matzke, Defects in ion-implanted uranium nitride, Physical Review B 41 (1990). [doi:10.1103/PhysRevB.41.3968](https://doi.org/10.1103/PhysRevB.41.3968).

- 781 [55] K. D. Johnson, D. A. Lopes, Grain growth in uranium nitride prepared by spark plasma
782 sintering, Journal of Nuclear Materials 503 (2018). [doi:10.1016/j.jnucmat.2018.02.041](https://doi.org/10.1016/j.jnucmat.2018.02.041).
- 784 [56] S. Nichenko, D. Staicu, Thermal conductivity of porous UO₂: Molecular dynamics study,
785 Journal of Nuclear Materials 454 (2014). [doi:10.1016/j.jnucmat.2014.08.009](https://doi.org/10.1016/j.jnucmat.2014.08.009).
- 786 [57] H. Matzke, Science of advanced LMFBR fuels, Elsevier Science Publishers B.V., 1986.
- 787 [58] M. Colin, M. Coquerelle, I. L. Ray, C. Ronchi, C. T. Walker, H. Blank, The sodium-
788 bonding pin concept for advanced fuels. Part I: Swelling of carbide fuel up to 12 [doi:10.13182/NT83-A33271](https://doi.org/10.13182/NT83-A33271).
- 790 [59] N. A. Javed, Oxygen solubility in uranium mononitride phase, Journal of the Less
791 Common Metals 29 (1972). [doi:10.1016/0022-5088\(72\)90186-5](https://doi.org/10.1016/0022-5088(72)90186-5).
- 792 [60] G. C. Jain, C. Ganguly, Experimental evaluation of oxygen solubility in UN, PuN
793 and (U, Pu)N, Journal of Nuclear Materials 202 (1993). [doi:10.1016/0022-3115\(93\)90394-E](https://doi.org/10.1016/0022-3115(93)90394-E).
- 795 [61] I. I. Konovalov, B. A. Tarasov, E. M. Glagovsky, Structural-phase state and creep of
796 mixed nitride fuel, in: IOP Conference Series: Materials Science and Engineering, Vol.
797 130, 2016. [doi:10.1088/1757-899X/130/1/012030](https://doi.org/10.1088/1757-899X/130/1/012030).
- 798 [62] B. J. Jaques, J. Watkins, J. R. Croteau, G. A. Alanko, B. Tyburska-Püsche, M. Meyer,
799 P. Xu, E. J. Lahoda, D. P. Butt, Synthesis and sintering of UN-UO₂ fuel composites,
800 Journal of Nuclear Materials 466 (2015). [doi:10.1016/j.jnucmat.2015.06.029](https://doi.org/10.1016/j.jnucmat.2015.06.029).
- 801 [63] D. R. Olander, A. T. Motta, Light Water Reactor Materials Volume II: Applications,
802 American Nuclear Society, 2021.